Plasma Electrodynamics and Applications

Academic and Research Staff
Professor Abraham Bers, Dr. Abhay K. Ram

Visiting Scientists and Research Affiliates
Dr. Chris N. Lashmore-Davies (EURATOM, United Kingdom Atomic Energy Authority, Culham Science Centre, Abingdon, Oxfordshire, U.K.), Dr. Yves Peysson (TORE-SUPRA, Commissariat à l'Énergie Atomique, Cadarache, France)

Graduate Students
Joan Decker, Ronald J. Focia, Ante Salcedo, David J. Strozzi

Undergraduate Students
Daniel S. Kim

Technical and Support Staff
Laura M. von Bosau

Introduction

The work of this group is concerned with phenomena relevant to controlled fusion energy generation in high-temperature plasmas that are confined magnetically or inertially, and phenomena in space plasmas. We report on six studies of the past year.

Sections 1 and 2 relate to modeling and understanding recent experiments on stimulated Raman backscattering from intense laser-plasma interactions of interest to inertial confinement fusion. Section 1 presents results from the concluding set of experiments carried out at, and in collaboration with, the Los Alamos National Laboratory. In last year's progress report[1] we summarized experiments in stimulated Raman scattering (SRS) that exhibited coupling to ion dynamics through the excitation of the Langmuir decay instability (LDI) and its cascades. Here we report on the continuation of these SRS experiments and the simultaneous observation of laser scattering off a new mode that seems to be an electron acoustic wave (EAW). Analytical and computational work carried out to understand these observations is also summarized. The experiments on SRS-LDI cascades and on SRS-EAW, and their modeling and interpretations, are detailed in the Ph.D thesis of Mr. Ronald J. Focia recently submmited by him to the EECS department.[2] Section 2 reports on the continuation of our work on modeling SRS and its coupling to LDI with the use of five nonlinear coupled mode equations. Depending upon the Landau damping strength of the electron plasma waves involved, two distinctly different saturation states were discovered and are described. This has also formed part of the PhD. thesis by Mr. Ante Salcedo, and has been recently submitted by him to the EECS department.[3]

Section 3 describes our renewed interest in the potential synergism of RF driven currents and bootstrap currents – a problem of importance to high-performance and steady-state operation of tokamak confined fusion plasmas. Our original work on this, summarized in a Ph.D. thesis from our

[1] R. J. Focia, A. Bers, and A. K. Ram, "Plasma Electrodynamics and Applications: Section 1 – Results of Recent Single Hot Spot Laser-Plasma Experiments at Los Alamos National Laboratory," *Progress Report No. 143,* MIT Research Laboratory of Electronics, Cambridge, 2001 (http://rleweb.mit.edu/Publications/pr143/Chapter-19-web.pdf).

[2] R. J. Focia, *Observation and Characterization of Single Hot Spot Laser-Plasma Interactions*, Ph.D. dissertation, Department of Electrical Engineering and Computer Science, MIT, February 2002.

[3] A. Salcedo, *Coupled Modes Analysis of SRS Backscattering, with Langmuir Decay and Possible Cascadings,* Ph.D. dissertation, Department of Electrical Engineering and Computer Science, MIT, December, 2001.

group,[4] was limited by a rather slow code. In collaboration with Dr. Yves Peysson from the TORE-SUPRA group in Cadarache, France, a new, fast, and fully implicit code was developed, and we report on it and the first new results from it.

Section 4 presents first results on the nonlinear, chaotic dynamics of ions in two electrostatic waves propagating obliquely to the magnetic field imposed on a plasma. This is a basic study problem on nonlinear and chaotic dynamics in plasmas. Previously,[5,6] we discovered the possibility of obtaining coherent energization of ions by two electrostatic waves propagating perpendicular to a magnetic field, with the potential for a new means of ion heating. Here we report first results for a more (experimentally) realistic case of two waves propagating obliquely to the magnetic field.

The work reported in Section 5 relates to modeling and understanding recent observations in space plasmas that show ion energization from localized fields in density depressions. Finally, Section 6 describes a general proof of symmetries in linear mode conversions of waves in an inhomogeneous plasma, and the consequences of such symmetries for plasma heating, and emission from plasmas, at various frequencies.

[4] S. D. Schultz, *Lower Hybrid and Electron Cyclotron Current Drive With Bootstrap Current in Tokamaks,* Ph.D. dissertation, Department of Physics, MIT, September, 1999.
[5] A. K. Ram, D. Bénisti, and A. Bers, "Ion Acceleration in Multiple Electrostatic Waves," *J. Geophys. Res.,* **103**, 9431 (1998).
[6] D. Bénisti, A. K. Ram, and A. Bers, "Ion Dynamics in Multiple Electrostatic Waves in a Magnetized Plasma – Part I: Coherent Acceleration," *Phys. Plasmas,* **5**, 3224 (1998); and D. Bénisti, A. K. Ram, and A. Bers, "Ion Dynamics in Multiple Electrostatic Waves in a Magnetized Plasma – Part II: Enhancement of the Acceleration," *Phys. Plasmas,* **5**, 3233 (1998).

1. Observation and Modeling of Stimulated Electron Acoustic Wave Scattering

Sponsors
Los Alamos National Laboratory (LANL) Contract E29060017-8F

Project Staff
R. J. Focia, Professor A. Bers, and Dr. A. K. Ram

This section presents observations of, numerical simulations of, and a theory for scattering off a new mode observed experimentally in a laser-produced plasma.[7] Scattering off of this new mode has been named *stimulated electron acoustic scattering* (SEAS) since the incident laser scatters off of an electron acoustic wave (EAW) to produce a scattered electromagnetic wave (EMW). The following is a summary of work outlined in a recent Ph.D. dissertation.[2]

A. *Experimental Observation of Stimulated Electron Acoustic Scattering*

In the recent single hot spot (SHS) experiments, stimulated scattering was observed at a frequency and phase velocity ($\omega \approx 0.4\omega_{pe}$, $v_\phi \approx 1.4v_e$) below that of the SRS generated electron plasma wave (EPW) and well above that of the ion acoustic wave (IAW). The motivation for the work presented here was to understand the origins of and scattering off of this new electron acoustic wave (EAW) mode. As it turns out, scattering off of this or a similar mode was observed in past experiments.[8,9] Although not understood, it was explained as resulting from either stimulated Raman scattering (SRS) from an abnormally low density region in the plasma, increased levels of ion mode activity, or non-uniform laser heating of the plasma. In the very homogeneous, well-characterized plasmas used in the SHS experiments, a low density region near the SHS interaction volume and non-uniform laser heating of the plasma would be extremely difficult to create and there is no possibility for an ion mode density fluctuation resulting in scattering at or even near this frequency.

However, it should be noted that scattering off the EAW mode is energetically insignificant when compared to the energy in the SRS EMW. This is shown by the time-integrated backscattered spectra shown in Figure 1. Due to the limited dynamic range of the streaked SRS spectrometer diagnostic, observation of both SRS and SEAS spectra on the same shot was not possible. Thus, Figure 1 is a composite of two separate shots having approximately the same laser and plasma conditions. The spectral resolution of the instrument is ~1.8 nm for the SRS spectra, and ~0.25 nm for the SEAS spectra. The spectrum shows a bright narrow peak at 654 nm (spectral width ~7 nm) corresponding to SRS scattering from an EPW with $k\lambda_{De} \approx 0.27$ ($T_e \approx 350 - 400$ eV). The SRS reflected energy was ~0.06 of the incident laser energy. Also shown is a spectrum recorded in the range from 540-600 nm on a separate shot with nearly identical laser and plasma conditions. A narrow peak was observed at 566.5 nm (spectral width ~5 nm), whose amplitude is ~3000x lower than the SRS peak – this is the EAW mode. The energy in the SEAS mode was at most 2×10^{-5} of the incident laser energy. Note that the dispersion of the EAW mode was not established experimentally.

[7] D. S. Montgomery, R. J. Focia, H. A. Rose, D. A. Russel, J. A. Cobble, J. C. Fernández, and R. P. Johnson, "First Observation of Stimulated Electron Acoustic Wave Scattering," *Phys. Rev. Lett.,* **87**, 155001 (2001).
[8] C. Labaune et al., "Large-Amplitude Ion Acoustic Waves in a Laser-Produced Plasma*," Phys. Rev. Lett.,* **75**, 248 (1995).
[9] J. A. Cobble et al.,"The Spatial Location of Laser-Driven, Forward-Propagating Waves in a National-Ignition-Facility-Relevant Plasma," *Phys. Plasmas,* **7**, 323 (2000).

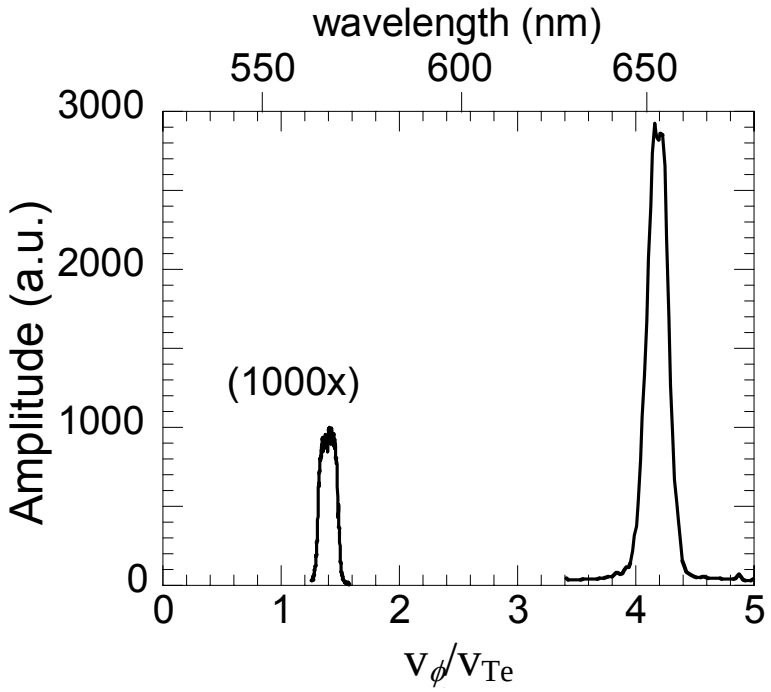

Figure 1: Composite image from two separate shots, at an intensity ~ 10^{16} W/cm^2, showing the time-integrated SRS and SEAS signals. The amplitude of the SEAS is seen to be approximately 3000x less than the SRS signal and occurs at a much lower phase velocity.

As characterization of SEAS was not the primary mission of the experiments, the only scaling performed was a variation of the interaction laser intensity. It was observed that at an intensity below I ≈ 3x10^{15} W/cm^2, the SEAS mode dropped below the detection threshold of the instrument while SRS was still observed at the 0.005 level. Due to the experimental setup, no other scaling studies were feasible. Thus, all that could be concluded is that there was a threshold for SEAS and that the frequency of the mode was known.

The phase velocity of the mode was estimated by assuming the scattering is a resonant process and *k*-matching the interaction. An example of resonance matching the SEAS interaction is shown in Figure 2 along with the SRS interaction. It is seen that since the frequency of the EAW mode is much lower than the laser and SRS EMWs, the difference in the wavenumber of the SRS and SEAS EMWs is very small. Thus, attempting to resolve these two EMWs in wavenumber was more difficult than resolving them in frequency. This will be elaborated on in more detail in the analysis of the numerical simulation data shown later.

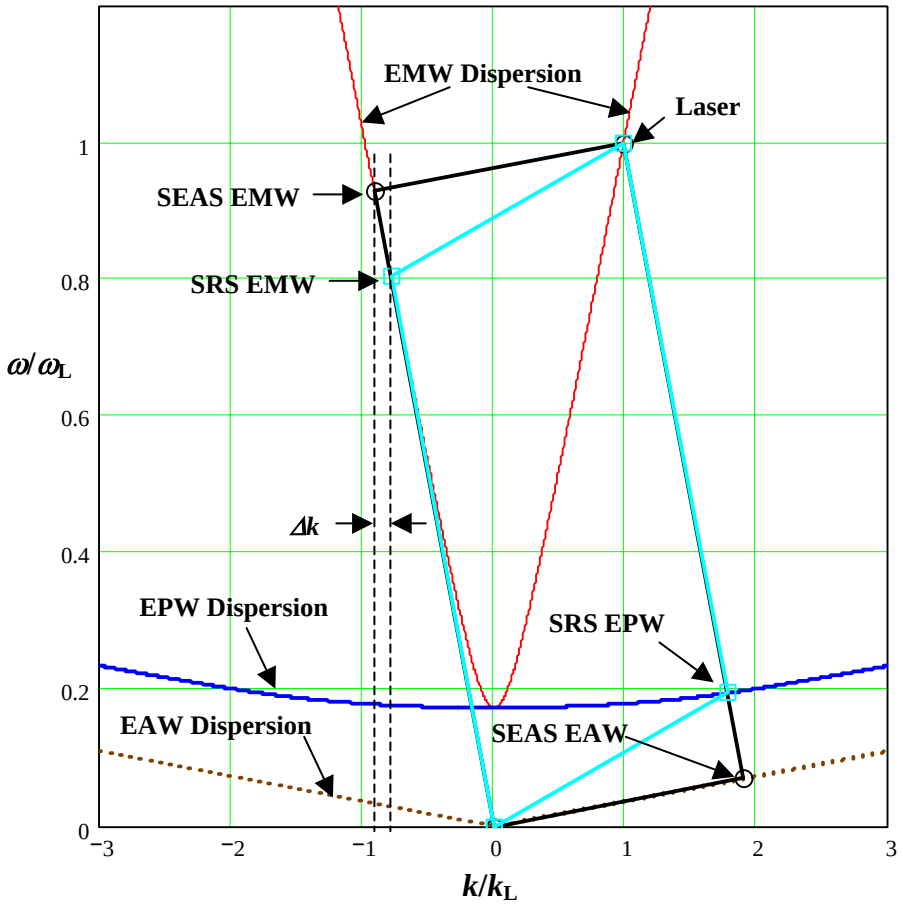

Figure 2: 1D resonance matching diagram showing the SRS and SEAS interactions. The phase velocity of the EAW dispersion has been set to that predicted by the experimental observation.

SEAS Mode Shot Analysis:						
Calibration information:			1-1800/500 nm grating			
			nm/pix:	0.03		
			Reference:	557.03	at pixel	662
Shot Number	**Energy (J)**	**I (W/cm^2)**	**$\Delta\lambda_{FWHM}$ (nm)**	**λ_{center} (nm)**	**R_{SRS} (%)**	**Δ t (ps)**
12807	0.35	4.185E+15	NA		NA	
12808	0.331	4.122E+15	4.71	565.925	6.61%	159.3
12809	0.244	3.831E+15	4.86	565.91	2.09%	157.5
12810	0.098	3.343E+15	NA		0.75%	
12826	0.152	3.524E+15	4.32	566.315	0.92%	168.2
12828	0.377	4.275E+15	NA		6.82%	
12829	0.51	4.719E+15	5.67	565.655	2.87%	134.5

Table 1: Summary of SEAS mode observations. Δt is the time duration of the observed spectrum.

The results of data analysis on the recent SEAS observations (Figure 1) are collected in Table 1. To summarize, the past and recent experimental observations of this mode show that:

- The frequency and phase velocity of the mode lies in between that of the EPW and the IAW,
- The energy in the scattered mode is much less that that in SRS,
- In the French experiments,[8] the frequency of the mode was observed to have a dependence on the interaction laser beam intensity,
- The recent SHS experiments noted little deviation in the frequency versus interaction laser intensity which may be due to the fact that SRS was saturated,
- The SEAS interaction exhibited a threshold intensity, and
- The scattering does not last as long in time as the SRS.

On a few shots the Thomson scattering diagnostic was set up to probe EPWs outside of the hot spot. The probe and collection geometry for these shots are shown in Figure 3. The spectra from these shots (c.f. Figure 4) show numerous spectro-temporal events possibly indicating that beaming electrons generated by SRS are interacting with the plasma outside the SHS and also give an approximate time duration of their interaction. The Thomson probe was carefully aligned to look outside of the interaction hot spot. However, it cannot be ruled out that the observed spectrum could also have been due to self-focusing and filamentation causing SRS past (i.e., in front of) the best focus position of the hot spot.[10] On shot 12831 the SRS spectrum (see Figure 4) is very broad and is not indicative of filamentation. On the other hand, distinct spectro-temporal events are noted in the streaked Thomson spectrum. An analysis of how far EPWs generated by SRS and electrons beaming at the EPW phase velocity could travel in the plasma was performed. The results of these calculations show that an EPW generated by SRS in the SHS would travel only ~2 μm before decaying in amplitude one e-folding due to Landau damping and thus would not make it to the Thomson probe point. However, the mean free path of a beaming electron is on the order of ~50 μm and thus, via a beam-plasma interaction, could be the source of the EPWs observed outside of the SHS.

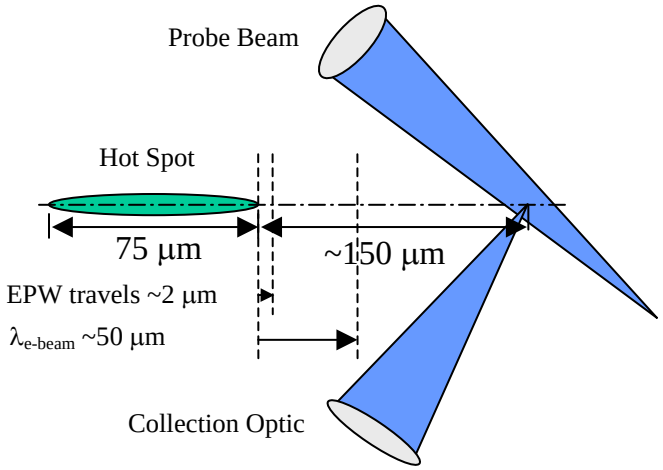

Figure 3: Hot spot and probe geometry for investigation of plasma waves outside of the SHS.

[10] D. S. Montgomery, R. P. Johnson, H. A. Rose, J. A. Cobble, and J. C. Fernández, "Flow-Induced Beam Steering in an Single Laser Hot Spot," *Phys. Rev. Lett.,* **84**, 678 (2000).

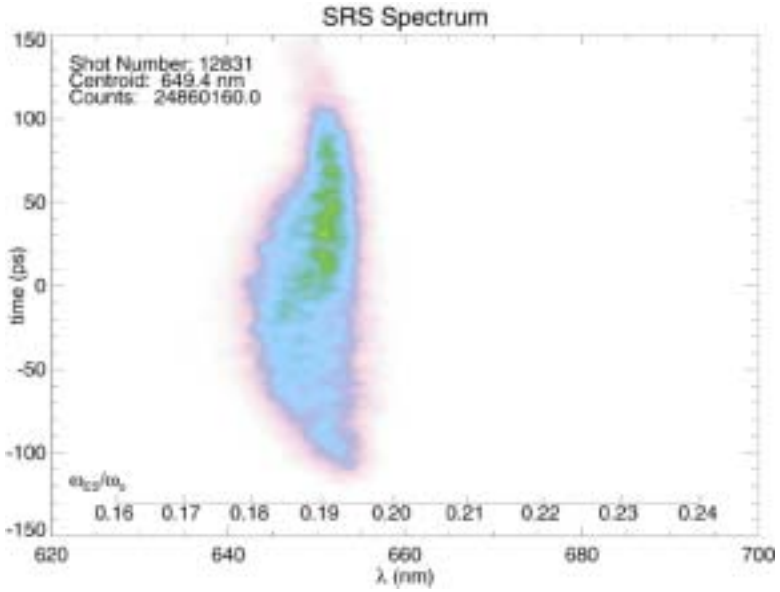

Figure 4: (a) SRS and (b) streaked Thomson spectra from shot 12831 where EPWs were probed outside of the SHS. The broad SRS spectrum does not directly correlate to the numerous spectro-temporal events observed in the streaked Thomson image. These EPWs could be the result of beaming electrons interacting with the plasma.

Some time scales must be evaluated when one considers that in the SHS experiments a plasma flow transverse to the interaction beam is introducing fresh plasma into the system on a continuous basis, and also that the streak camera diagnostic integrates over a small but finite period of time. These time scales must be considered because, as the plasma system evolves nonlinearly, any phase space structure may be washed out due to quasilinear diffusion or some other effect. The transverse flow velocity at a distance of $z \approx 400\ \mu m$ ($n/n_c \approx 0.03$) from the target is $v_z \approx 6 \times 10^7$ cm/s.[2] Considering that the width of the single hot spot in the direction of the transverse flow is $w \approx 2.4\ \mu m$, the plasma will be completely swept out of the SHS in a time $t \approx 4$ ps, and fresh plasma is being swept into the SHS on a continuous basis. The SRS streak camera CCD had 1024x1024 pixels and

the streak time for the EAW shots was 2 ns. Thus, each pixel actually gives a time-integrated picture over a period of ~2 ps. What these time scales show is that processes could be occurring in the plasma on a time scale much less than the integration time of the streak camera diagnostic CCD and they could never be resolved. If the process is transient but resurrected due to a continuous supply of fresh plasma, the time integration of the diagnostic will provide a picture that makes the process appear to be continuous.

B. *Numerical Simulation of SRS Using a 1D Vlasov Code*

Numerical modeling using a relativistic, one-dimensional (1D), finite-length, Eulerian-Vlasov code with mobile electrons and a single species (also mobile) hydrogen ions was used to investigate the nonlinear time evolution of the electron distribution function during SRS. This code, with various boundary conditions and dimensionalities, has been used extensively in the past to simulate SRS and beat-wave phenomena.[11,12,13,14,15,16] The equations solved and numerical methods employed are described in more detail in [2].

Parameters typical of the regime where SEAS was observed were specified as inputs to the Vlasov code: I_o = 2x10^{15} W/cm^2 (unfortunately just below the observed threshold), λ_L = 527 nm, L_{system} = 164.5 (c/ω_p) (plasma region ~75 μm), T_e = 350 eV, T_i = 100 eV, n_e/n_c = 0.032, γ_{SRS}/ω_L = 0.004 (SRS growth rate), γ_{cSRS}/ω_L = 0.00023 (SRS convective threshold). Although the plasma in the experiment was 50/50 carbon-hydrogen (CH), the Vlasov code is limited to modeling only a hydrogen plasma. The effects of this limitation will primarily be manifested in the IAW damping which may affect SRS through LDI but this is not considered here.

For convenience in the calculations, the code normalizes all parameters. Frequencies are normalized to the electron plasma frequency ω_{pe}; wavenumbers are normalized to the free space plasma wavenumber $k_{pe} = \omega_{pe}/c$, where c is the speed of light; electric and electromagnetic fields are normalized to $\omega_{pe} m_e c/e$; time is normalized to the inverse of the electron plasma frequency; and momentum is normalized to $m_e c$. For the above parameters, the results anticipated from the simulation (in normalized units) are: ω_L = 5.59, ω_{SRS} = 4.477, ω_{EPW} = 1.113, k_o = 5.5, $|k_{SRS}|$ = 4.364, k_{EPW} = 9.864, $P_{\phi EPW}$ = 0.114.

Since the Vlasov code is essentially noiseless,[12] it was necessary to add an initial perturbation. This imposed initial distribution function was chosen to be $f(p) \sim \exp\left\{-(1/2)\left[(p/p_{th}) - \varepsilon\cos(k_{EPW}x)\right]^2\right\}$ with $\int f(p)dp = n_0$, $k_{EPW} \approx 9.9$, in normalized units, and ε = 0.05. This is equivalent to initially imposing a current density $J = q\, n_0\, v_{Te}\, \varepsilon \cos(k_{EPW}\, x)$

[11] A. Ghizzo et al., "A Vlasov Code for the Numerical Simulation of Stimulated Raman Scattering," *J. Comput. Phys.,* **90**,431 (1990).
[12] P. Bertrand et al., "A nonperiodic Euler-Vlasov code for the numerical simulation of laser-plasma beat wave acceleration and Raman scattering," *Phys. Fluids B,* **2**, 1028 (1990); when conducting initial simulations using the Vlasov code, it was found that when no initial perturbation was added there was no evolution of SRS.
[13] A. Ghizzo et al., "Comparison between 1D and 1 ½ D Eulerian Vlasov Codes for the Numerical Simulation of Simulated Raman Scattering," *J. Comput. Phys.,* **102**, 417 (1992).
[14] P. Bertrand et al., "Two-stage electron acceleration by simultaneous stimulated Raman backward and forward scattering," *Phys. Plasmas,* **2**, 3115 (1995).
[15] M. L. Bégué, A. Ghizzo, and P. Bertrand, "Two-Dimensional Vlasov Simulation of Raman Scattering and Plasma Beatwave Acceleration on Parallel Computers," *J. Comput. Phys.,* **151**, 458 (1999).
[16] A. Ghizzo et al., "Trajectories of Trapped Particles in the Field of a Plasma Wave Excited by a Stimulated Raman Scattering," *J. Comput. Phys.,* **108**, 373 (1993).

which in the first time step, $\Delta t = 0.0047$ in normalized units, leads to a density perturbation $(\delta n / n) \approx 6 \times 10^{-5}$. Independently of the laser, this density perturbation grew very rapidly (apparently due to the imposed edge boundary conditions[17] and the relatively large initial current density) to form a trapped electron distribution around the phase velocity of the thus engendered electron plasma wave. Such a distribution, which appeared independent of the laser, is shown in Figure 5 taken at a time $\tau \approx 51.7$ (ω_{pe}^{-1}). This time corresponds to 0.08 ps while the SRS growth time is only 0.07 ps. Thus, although in this time the laser has traversed about one-third of the simulation box, SRS had barely a chance to grow. However, the laser would scatter off of the density fluctuations which were there, engendered by the imposed initial distribution function. Figure 6 shows the spectral content of the electromagnetic and electrostatic fields at time $\tau \approx 197.4$ (ω_{pe}^{-1}), or in actual time 0.32 ps, when the laser has propagated about 1.2 times the length of the simulation box. Note from Figure 6 that at this time (corresponding to about 4.4 SRS growth times), the peaks for the laser, the SRS EMW, and the initially driven EPW are at k_o = 5.492, $|k_{SRS}|$ = 4.362, and k_{EPW} = 9.893, respectively. This agrees closely with what resonance matching was predicted by the SRS interaction, but the intense EPW here was not produced by laser engendered SRS.

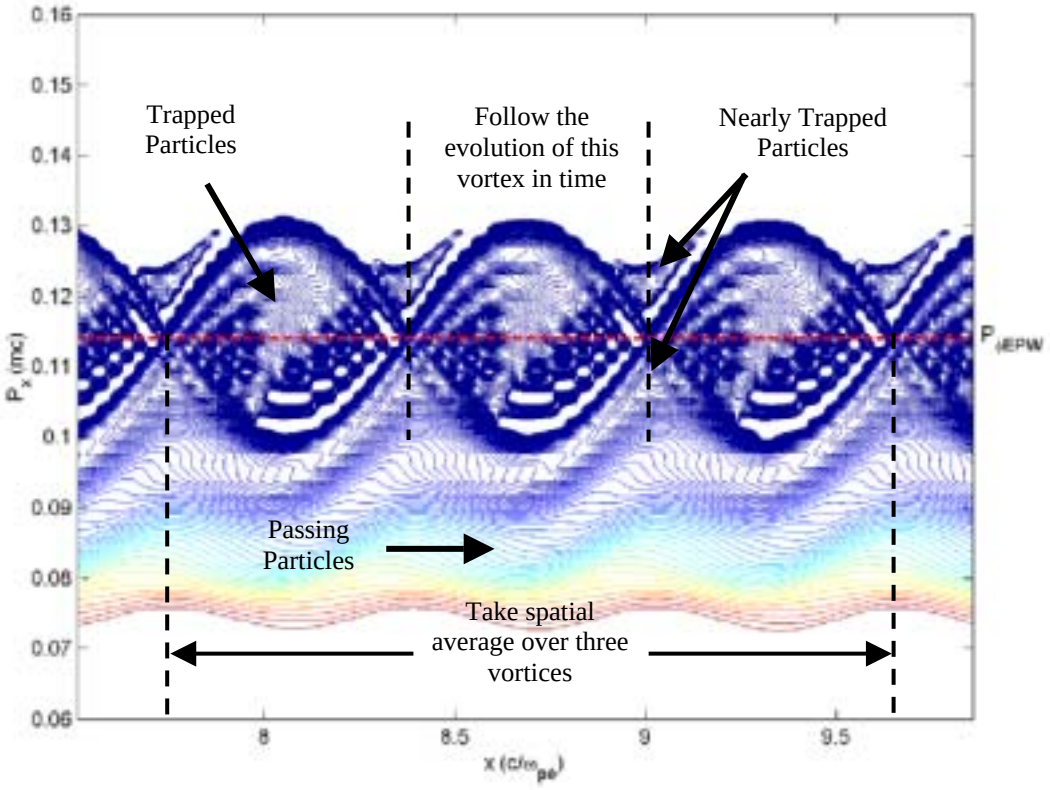

Figure 5: Snapshot at time $\tau \approx 51.7$ (ω_{pe}^{-1}) of a region in phase space showing the formation of vortices.

[17] Due to the way that the total charge in the system is divided equally and placed at the boundaries there is always some initial noise in the system. A spectral analysis of this noise revealed that it was in a very low frequency range and not appropriate to excite SRS.

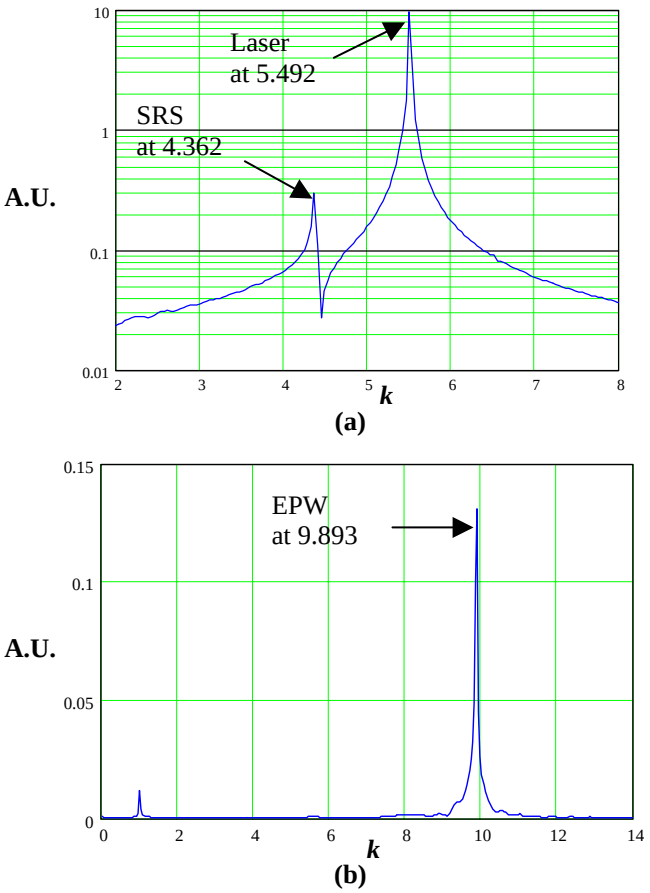

Figure 6: Spectral content of (a) the electromagnetic and (b) the electrostatic fields in the simulation box when the laser has propagated the simulation box ~1.2x [$\tau \approx 197$ (ω_{pe}^{-1})].

To get an idea of how the electron distribution evolves in time, one region in phase space was followed as it was moving at the phase velocity of the EPW. From the initial picture of phase space shown in Figure 5, the vortex centered at x ≈ 8.7 was followed in a frame moving at the phase velocity of the EPW ($v_{\phi EPW} \approx 0.113$ c). In order to ascertain how the time-evolved electron distribution deviates from the initial Maxwellian, a spatial average was taken over approximately three plasma wave wavelengths (or vortices). Spatially averaging the time-evolved distribution function was necessary in order to analyze the distribution function in momentum space. As seen in Figure 7(a), the time-evolved distribution differs very slightly from the initial Maxwellian. Since this difference is so small, one cannot get a quantitative feel for it unless the initial Maxwellian is subtracted from the time-evolved distribution function. Figure 7(b) shows the deviation, or δf_e, of the time-evolved distribution function from the initial Maxwellian.

As seen in Figure 7, a relatively small percentage of the bulk particles are being redistributed to momenta higher than P_ϕ; most of them are at momenta below P_ϕ. The time-evolved electron distribution may be effectively modeled by a Maxwellian with a slightly lower density (compared to the initial Maxwellian) combined with a beam-like structure below P_ϕ that is nearly Maxwellian. The behavior at this stage in the evolution is a little noisy in momentum space. As time progresses and the system evolves, this becomes more smoothed out. This is essentially the striking result of the simulations. That is, the time-evolved electron distribution is no longer Maxwellian but can be crudely approximated by a slightly lower density Maxwellian (relative to the

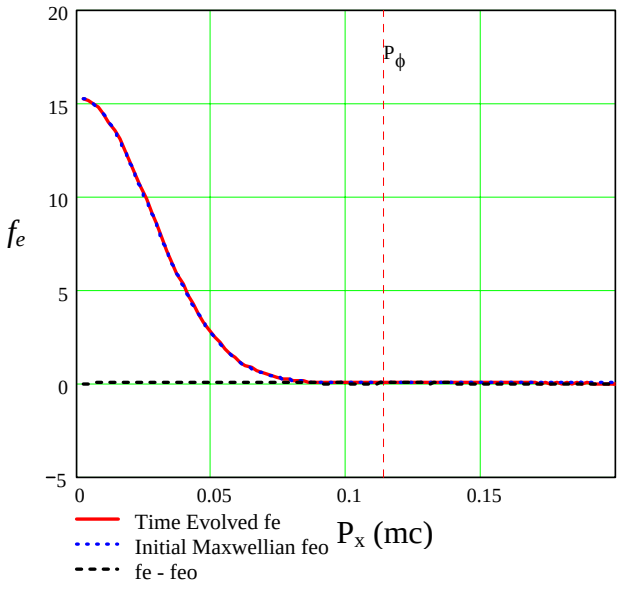

(a)

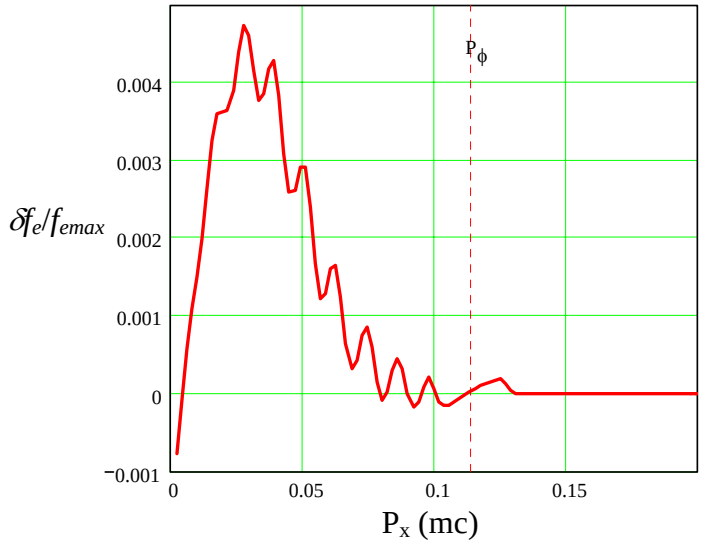

(b)

Figure 7: (a) Spatial average of the electron distribution over three vortices at $\tau \approx 51.7$ (ω_{pe}^{-1}) centered on $x \approx 8.7$ (c/ω_{pe}). (b) The deviation from the initial Maxwellian (normalized to the maximum of the time-evolved distribution) shows a redistribution of particles mainly toward momenta below the driven EPW phase velocity.

initial Maxwellian) and a low density beam-like structure with a velocity less than the phase velocity of the driven EPW.

The 1D Vlasov code also has the elements necessary to predict scattering off of the EAW mode, should it exist. The *k*-space spectrum for the specified simulation parameters (see Figure 6) shows that SRS is occurring where expected. However, resonance matching predicts that the wavenumbers of the EMWs from SRS and SEAS will be very close in magnitude (see Figure 2). Additionally, the experimental observation shows that the amplitude of the SEAS mode is ~3 orders

of magnitude less in intensity than that of SRS. Thus, looking at the *k*-space spectrum would most likely not reveal the mode. In order to ascertain whether or not the code will predict the SEAS mode self-consistently, the forward and backward propagating EMWs are saved at the boundaries of the plasma region at each time step. This data is Fourier analyzed to provide the frequency spectrum of the scattered light wave. Resonance matching predicts that the frequency difference between the SEAS and SRS modes should be discernable even for disparate amplitudes. Figure 8 shows the frequency spectrum of the backscattered EMWs at time τ = 128 (ω_{pe}^{-1}) and there is structure in the region where the EAW mode is observed. The behavior of the spectral structure was bursty in time throughout the simulation and does not appear after a time $\tau \approx 160$ (ω_{pe}^{-1}). As will be shown in the next section, the damping of this mode is expected to be large compared to the SRS EPW (since it is a quasimode) and the growth rate for the SEAS interaction will be much less than the SRS one. We take Figure 8 as evidence that the Vlasov code is showing SEAS, albeit from a (trapped)

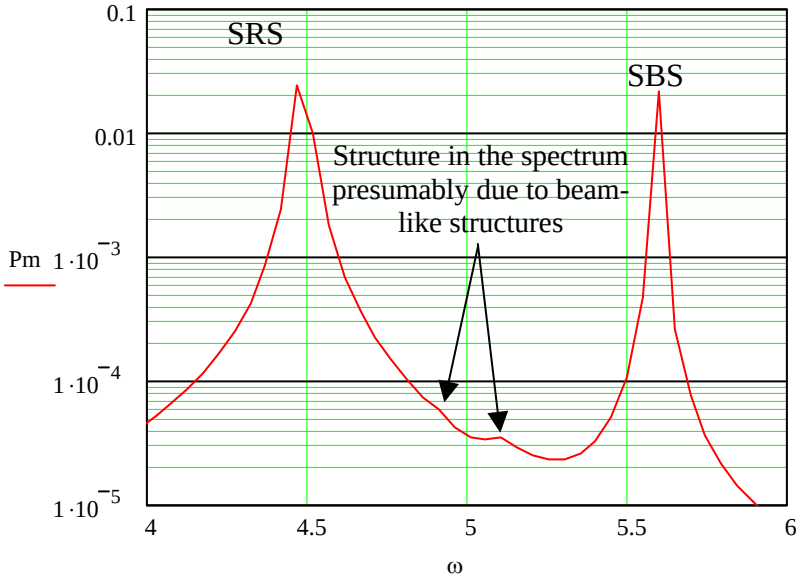

Figure 8: Fourier spectrum of the backward propagating EMW passing the left-hand boundary of the plasma region at time τ = 128 (ω_{pe}^{-1}).

electron distribution that was imposed rather than one that evolved from saturated SRS.

C. *Description of SEAS as Laser Scattering off a Bi-Maxwellian Electron Distribution*

Explanations for SEAS have been presented previously in the literature.[7,18] In this subsection, an alternate explanation for SEAS is presented. The Vlasov-Maxwell code results of the previous section show that, starting with a trapped electron distribution function around the phase velocity of an engendered EPW (which may correspond to an SRS saturated EPW), laser scattering off of this electron distribution produces backscattered EMWs at frequencies of SRS and above, the latter being consistent with SEAS [see Figure 6(a) and Figure 8]. Furthermore, the spatially averaged electron distribution function, associated with the large amplitude EPW, exhibits a weak, thermally spread beam at velocities below the phase velocity of the large amplitude EPW. This feature was found to persist for times comparable to the transit time of the laser, and it suggests that an electron distribution function consisting of a bulk Maxwellian and such a beam may exhibit an electrostatic mode of an appropriate EAW off of which laser scattering would produce the SEAS-EM wave. To investigate this, we first investigated the appearance of a natural mode or quasi-mode of EAW-type

[18] H. A. Rose, "A self-consistent trapping model of driven electron plasma waves and limits on stimulated Raman scatter," *Phys. Plasmas,* **8**, 4784 (2001).

in an appropriate bi-Maxwellian plasma,[2,19] and then calculated laser scattering off such a mode/quasi-mode. Laser scattering off this distribution occurs on a time scale on which presumably (although so far not proven) the distribution from the nonlinear evolution of SRS can be taken as a new equilibrium distribution that exhibits a low density, thermally spread, beam structure. One possible explanation for the EAW is that it is a linear, weakly damped mode of a plasma whose electron distribution function contains a low density, thermally spread, beam structure. Thus, the observation of SEAS can be explained as a wave-wave (quasi-mode) interaction of the laser with a linear EAW whose existence depends on the non-linearly evolved electron distribution in SRS. Based on the above, we first establish that the presumed SRS evolved electron distribution function supports a self-consistent linear EAW[2,19] mode (or quasi-mode). We thus calculate the nonlinear scattering of the laser off of this EAW to explain the observed SEAS.

Using a bi-Maxwellian electron distribution function to model the SRS evolved beam-plasma system, the fully kinetic dispersion relation governing the relevant one-dimensional linear dynamics of this system is

$$D_L(K,\Omega) = 1 - \frac{1}{2K^2} Z'\left(\frac{\Omega}{\sqrt{2}K}\right) - \frac{1}{2K^2}\frac{n_b}{n_e}\frac{T_e}{T_b} Z'\left(\frac{\Omega}{\sqrt{2}K}\sqrt{\frac{T_e}{T_b}} - \frac{\mathrm{V}_b}{\sqrt{2}}\right) = 0 . \qquad (1)$$

where the ion dynamics have been neglected, and $\Omega = \omega/\omega_{pe}$, $K = |k|\lambda_{De}$, and $\mathrm{V_b} = \mathrm{v}_b/\mathrm{v}_{Tb}$; the bulk electron plasma is characterized by density n_e and temperature T_e, and the beam by density n_b, temperature T_b, and drift v_b. Solving for the roots of (1), the frequency (normalized to the background electron plasma frequency) versus $k\lambda_{De}$, the wave vector magnitude times the background electron Debye length is obtained. Equation (1) was solved using Mathcad and a *Z*-function solver created from IMSL routines. Parameters gleaned from experimental data from the SEAS shots of the recent experiments were used to explore the effect on the damping and dispersion of the Landau roots. To reiterate, on these shots scattering, presumably stimulated, off of a mode having a normalized frequency $\Omega \approx 0.4$ was observed. The measured electron temperature was $T_e \approx 390$ eV (this is the background electron temperature in our bi-Maxwellian model). The plasma density is approximated from the SRS spectrum on similar shots and is found to be $n_e/n_{crit} \approx 0.03$. For the approximate plasma density and background electron temperature, the wavenumber times Debye length is $k\lambda_{De} \approx 0.28$. We do know the frequency of the SEAS mode but did not experimentally determine its dispersion. The parameters of the bi-Maxwellian model were then varied in order to obtain a weakly damped root that passes through the observed data point.

Interesting results emerge when we consider that the trapped electrons comprise a relatively weak beam, below the SRS-EPW phase velocity, as seen in the (not fully self-consistent) evolved Vlasov simulation. In this case it is possible to obtain two weakly damped roots at approximately the correct frequencies of the SRS driven EPW and the EAW observed in the experiments. Figure 9 shows the zero contours of (1) at K = 0.28 with parameters $T_e = 390$, $T_b = 20$, $n_e = .97$, $n_b = 0.03$, $V_b = 7.42$ ($\sim 0.4 v_{\phi EPW}$). What this shows is that a small percentage of electrons comprising a beam with a small thermal spread can leave the driven EPW root only slightly modified and also introduce a weakly damped EAW mode. If the beam velocity is sufficiently separated from the phase velocity of the driven EPW or if the beam density is very small, calculations have shown that the beam has little effect on the EPW mode. This is the major new result. The bi-Maxwellian model shows that electrons beaming through the background plasma are one possible explanation for the existence of an EAW quasi-mode. Note that the beam parameters used to generate Figure 9(a) were chosen to produce a weakly damped EAW mode at the frequency observed in the experiments.

[19] Independently, and in a completely different context, EAW have been previously studied. See S. P. Gary, "Electrostatic Instabilities in Plasmas With Two Electron Components," *J. Geophys. Res.,* **90**, 8213 (1985).

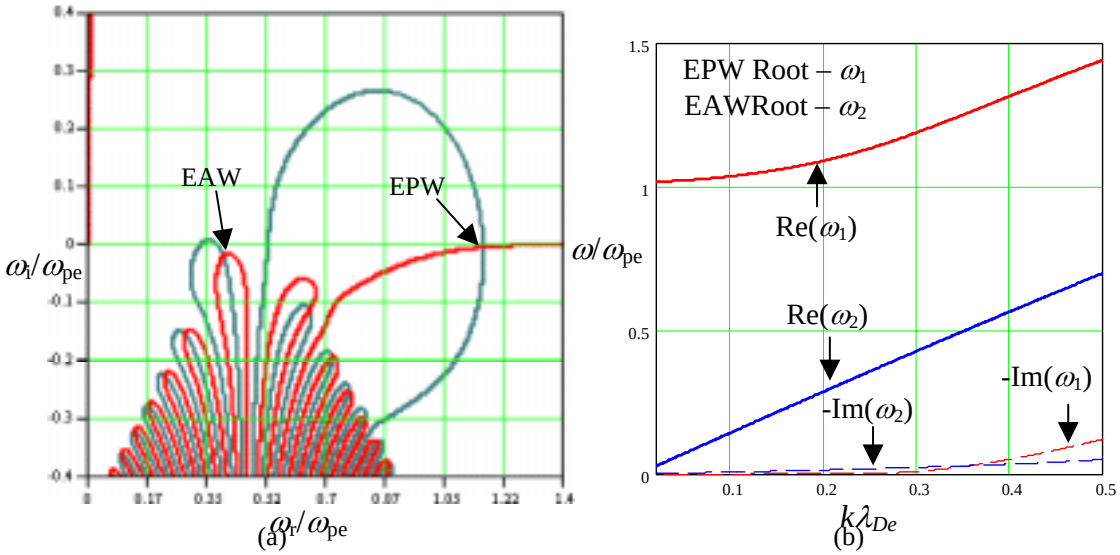

Figure 9: (a) Zero contours of (1) in the complex ω-plane for a bi-Maxwellian plasma with parameters T_e = 390, T_b = 20, n_e = .97, n_b = 0.03, V_b = 7.42 (~0.4$v_{\phi EPW}$). (b) Dispersion of the electron plasma wave and weakest damped electron acoustic root.

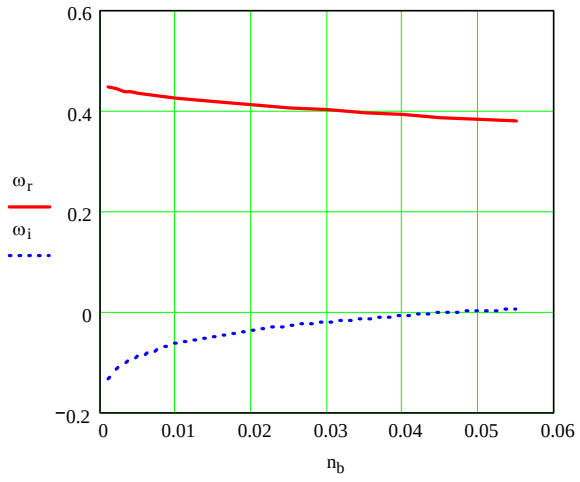

Figure 10: Plot of the frequency and damping of the EAW mode versus beam density fraction for the parameters T_e = 390, T_b = 20, V_b = 7.42 (~0.4$v_{\phi EPW}$), and $k\lambda_{De}$ = 0.28.

The effect of the beam density on the frequency and damping of the EAW mode is shown in Figure 10. For the parameters used to generate Figure 9(a), it is seen that for larger beam density fractions the EAW mode becomes less damped. Even for very small beam density fractions the mode is not too heavily damped. Thus, the number of particles necessary to produce this mode is very small. An important remaining question is whether the electron distribution function in unstable or saturated SRS actually exhibits the required beam to give rise to the appropriate EAW mode/quasi-mode. At this stage, from the Vlasov-Maxwell simulations carried out so far (see previous sub-section), we have only the indication that a large amplitude EPW engendered by initial conditions of a spatially

periodic current, rather than an SRS instability exhibits (transiently, but for sufficient time for laser scattering) a weak, thermally spread beam below the phrase velocity of the EPW.

Finally, we analyze the nonlinear scattering of the laser off of the modes/quasi-modes in a plasma containing a weak electron beam as exhibited in the dispersion relation (1). To account for the Landau damping of these modes and quasi-modes, a kinetic analysis of the scattering must be carried out, particularly for quasi-modes which we found the EAWs to be. Such an analysis is well-known and straightforward,[2] and yields the following nonlinear dispersion relation:

$$D_L = \frac{1}{4} k^2 \mathbf{v}_o^2 (-\chi_{Le}) \left(\frac{1}{D_{T+}} + \frac{1}{D_{T-}} \right) \tag{2}$$

where D_L is the kinetic linear dispersion function (i.e., the linear longitudinal permitivity function K) in (1), $\chi_{Le} = (D_L - 1)$ is the linear electron susceptibility function, v_0 is the electron's quiver velocity in the laser E-field, and $D_{T\pm} = (\omega \pm \omega_0)^2 - \omega_{pe}^2 - c^2 (k \pm k_0)^2$ is the up and down shifted electromagnetic dispersion function, with k_0 and ω_0 the laser wavenumber and frequency, respectively. Using parameters as shown in the illustration in Figure 9, which exhibits the linear mode/quasi-mode of EPW and EAW, we calculated the temporal growth rates by solving (2) for both SRS and SEAS. These are given in Figure 11, which also displays the linear modes/quasi-modes appearing as peaks in a plot $(1 / |K_L|) = (1 / |D_L|)$ vs. (v_ϕ / v_{Te}). A Maxwellian plasma with no beam component (dashed curve) exhibits a peak only at the phase velocity of the linear EPW. Including an appropriate beam component, as in the example of Figure 9, gives rise to the peak at the lower phase velocity of the linear EAW quasi-mode (solid curve). The SEAS growth rate is seen to be lower than the SRS growth rate by about an order of magnitude.

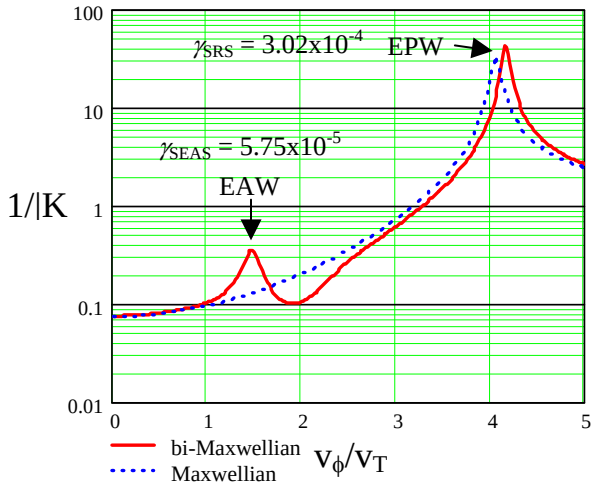

Figure 11 Plot of the inverse of the longitudinal permittivity function showing the difference between the Maxwellian and bi-Maxwellian models. For the parameters $K = k\lambda_{De} = 0.28$, T_e = 390 eV, T_i = 100 eV, T_b = 20 eV, n_e = .97, n_b = 0.03, V_b = 7.6 (~$0.4 v_{\phi EPW}$), and $I_o = 2 \times 10^{15}$ W/cm^2 the bi-Maxwellian model predicts the emergence of the EAW mode where observed experimentally. Growth rates are normalized to the laser frequency.

2. Coupling of Stimulated Raman Backscattering With the Langmuir Decay Interaction

Sponsors
Los Alamos National Laboratory (LANL) Contract E29060017-8F

Project Staff
A. Salcedo, Professor A. Bers, and Dr. A. K. Ram

We have investigated stimulated Raman backscattering observed in recent experiments that pertain to understand laser-plasma interactions in inertial confinement fusion (ICF). The nonlinear evolution of stimulated Raman scattering (SRS) is a parametric instability, in which the laser's electromagnetic wave (which we refer as the LASER) couples to an electron plasma wave (EPW) and a scattered electromagnetic wave. The largest growth rate of the scattered electromagnetic wave occurs in the backward direction (BEMW). Recent experiments aimed at understanding the backscattering in simple laser-plasma conditions suggest that SRS couples to the Langmuir decay interaction (LDI), which is a secondary parametric instability. In LDI the electron plasma wave excited by SRS couples to a backscattered electron plasma wave (BEPW) and an ion acoustic wave (IAW).

Considering a weak nonlinear interaction, we use the coupled mode equations (COM) to model the interaction between the slowly varying amplitudes of the LASER, BEMW, EPW, BEPW and IAW (a_1, a_2, a_3, a_4 and a_5, respectively):

$$(\partial_t + \mathrm{v}_{g1}\partial_x + \nu_1)\, a_1 = -\mathrm{K}_{SRS} a_2 a_3, \tag{3}$$

$$(\partial_t + \mathrm{v}_{g2}\partial_x + \nu_2)\, a_2 = \mathrm{K}_{SRS} a_1 a_3, \tag{4}$$

$$(\partial_t + \mathrm{v}_{g3}\partial_x + \nu_3)\, a_3 = \mathrm{K}_{SRS} a_1 a_2 - \mathrm{K}_{LDI} a_4 a_5, \tag{5}$$

$$(\partial_t + \mathrm{v}_{g4}\partial_x + \nu_4)\, a_4 = \mathrm{K}_{LDI} a_3 a_5, \tag{6}$$

$$(\partial_t + \mathrm{v}_{g5}\partial_x + \nu_5)\, a_5 = \mathrm{K}_{LDI} a_3 a_4. \tag{7}$$

In these equations, $|a_\ell|^2 = \mathrm{W}_\ell/\omega_\ell$, W_ℓ, $\mathrm{v}_{g\ell}$ and ν_ℓ are the wave action density, wave energy density, group velocity and damping rate of the ℓ th mode (with subscript $\ell = 1..5$, for the LASER, BEMW, EPW, BEPW and IAW, respectively). The coupling coefficients are:

$$\mathrm{K}_{\mathrm{SRS}} \approx \sqrt{\frac{2}{\varepsilon_o}}\frac{e}{m_e}\frac{k_3}{4}\left(\frac{\omega_{pe}^2}{\omega_1\omega_2\omega_3}\right)^{1/2}, \qquad \mathrm{K}_{\mathrm{LDI}} \approx \sqrt{\frac{2}{\varepsilon_o}}\frac{e}{m_e}\frac{\omega_{pe}}{4\mathrm{v}_{Te}}\left(\frac{\omega_5}{\omega_3\omega_4}\right)^{1/2};$$

where $\omega_{pe}^2 = q^2 n_e/\varepsilon_o m_e$ is the electron plasma frequency, $\mathrm{v}_{Te}^2 = \kappa T_e/m_e$ is the electron thermal velocity, and (ω_ℓ, k_ℓ) are the real frequency and real wave number of the ℓ th mode.

Equations (3)–(7) are normalized with: $a_\ell \leftarrow a_\ell/a_o$, $t \leftarrow \gamma_b t$, $x \leftarrow \gamma_b x/\mathrm{v}_{g3}$, $\mathrm{v}_{g\ell} \leftarrow \mathrm{v}_{g\ell}/\mathrm{v}_{g3}$ and $\nu_\ell \leftarrow \nu_\ell/\gamma_b$ [where $\gamma_b = |\mathrm{K}_{LDI}|a_o$, and a_o is the unperturbed amplitude of the laser]. The normalized five wave coupled mode equations (5COM) are:

$$(\partial_t + \mathrm{v}_{g1}\partial_x + \nu_1)\, a_1 = -\mathrm{G} a_2 a_3, \tag{8}$$

$$(\partial_t + \mathrm{v}_{g2}\partial_x + \nu_2)\, a_2 = \mathrm{G} a_1 a_3, \tag{9}$$

$$(\partial_t + \mathrm{v}_{g3}\partial_x + \nu_3)\, a_3 = \mathrm{G} a_1 a_2 - a_4 a_5, \tag{10}$$

$$(\partial_t + \mathrm{v}_{g4}\partial_x + \nu_4)\, a_4 = a_3 a_5 , \tag{11}$$

$$(\partial_t + \mathrm{v}_{g5}\partial_x + \nu_5)\, a_5 = a_3 a_4 . \tag{12}$$

where $G = \left|\mathrm{K}_{SRS} / \mathrm{K}_{LDI}\right|$ is the normalized SRS growth rate.

We have solved Equations (8) – (12) within a finite region of interaction, considering typical parameters from recent single hot-spot experiments.[20] We assume a laser wavelength $\lambda_o \approx 527\ nm$, laser intensity $I_o \approx 6\times10^{15}\ Watts/cm^2$, and the plasma parameters (T_e, T_i and n_e / n_{cr}) shown in Table 2. The corresponding normalized parameters $k_3\lambda_{De}$, ν_3, ν_4, ν_5 and G, are also provided in the table. The normalized group velocities are: $\mathrm{v}_{g1} \approx -\mathrm{v}_{g2} \approx 30$, $\mathrm{v}_{g3} \approx -\mathrm{v}_{g4} = 1.0$, and $\mathrm{v}_{g5} \approx 0$.

n_e/n_{cr}	T_e (keV)	T_i (keV)	ω_1/ω_{pe}	ω_2/ω_{pe}	$k_3\lambda_{De}$	ν_3	ν_4	ν_5	G
0.05	0.72	0.165	4.47	3.35	0.283	0.146	0.0816	0.0792	0.6199
0.043	0.71	0.162	4.82	3.68	0.308	0.257	0.165	0.0813	0.5882
0.04	0.7	0.16	5	3.85	0.319	0.314	0.21	0.0822	0.5724
0.036	0.7	0.156	5.27	4.11	0.339	0.433	0.311	0.082	0.5535
0.033	0.7	0.15	5.5	4.32	0.356	0.547	0.411	0.08	0.5389
0.03	0.7	0.145	5.77	4.47	0.375	0.685	0.535	0.08	0.5228
0.027	0.7	0.142	6.08	4.58	0.398	0.851	0.687	0.0811	0.5046
0.025	0.7	0.14	6.32	5.09	0.416	0.98	0.808	0.082	0.4915
0.023	0.7	0.136	6.59	5.34	0.435	1.13	0.949	0.081	0.478
0.015	0.7	0.117	8.16	6.78	0.548	1.99	1.78	0.081	0.4117

Table 2: Parameters for numeric simulations of experiments in [20].

Since ν_5 and G are almost constant, our investigation pertains to the SRS reflectivity as a function of $k_3\lambda_{De}$ (i.e., the damping of electron plasma waves). We find that SRS reaches a saturated state in a time that is much shorter than the duration of the laser pulse ($\approx 200 p\,\mathrm{sec}$).

In the saturated state, we find three different regimes that can be classified as: (1) strong EPW damping ($k_3\lambda_{De} > 0.4$), (2) intermediate EPW damping ($0.3 < k_3\lambda_{De} < 0.4$), and (3) weak EPW damping ($k_3\lambda_{De} < 0.3$). To illustrate the nature of such regimes of saturation, we show numerical results corresponding to $k_3\lambda_{De} = 0.4$, $k_3\lambda_{De} = 0.319$ and $k_3\lambda_{De} = 0.28$.

We consider a finite-plasma length of $250\ \mu m$, in normalized units spanning from $x = -450$ to $x = 450$. With the laser entering the plasma at $x = -450$, Figure 12 shows the amplitude of the backscattered electromagnetic wave $a_2(x = -450,\ t)$. Since the group velocities of the LASER and the BEMW have approximately the same magnitude, the calculation of the SRS reflectivity is straightforward:

[20] J. C. Fernández, J. A. Cobble, D. S. Montgomery, and M. D. Wilke, "Current Status of Laser-Matter Interaction Experimental Research at Los Alamos National Laboratory", in *Proceedings of the XXVI European Conference on Laser Interaction with Matter (ECLIM)*, Prague, Czech Republic, June 12–16, 2000.

$$SRS_r = \frac{\omega_2}{\omega_1}\left(\frac{a_2(-450,t)}{a_1(-450,t)}\right).$$

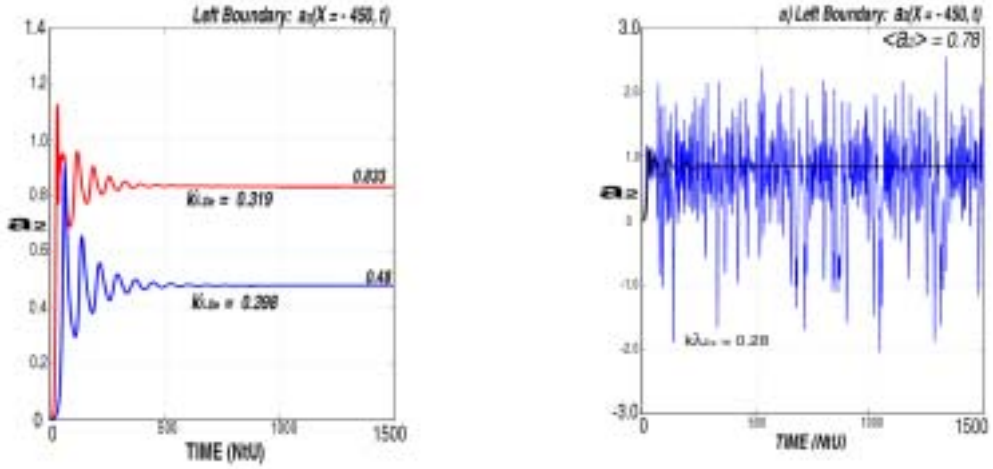

Figure 12: Time variation of the backscattered electromagnetic field $a_2(-450,t)$.

In Figure 12(a), the backscattered field amplitudes $[a_2(-450,t)]$ in the strong ($k_3\lambda_{De} = 0.4$) and intermediate ($k_3\lambda_{De} = 0.319$) EPW damping regimes are found to reach constant amplitudes in $t < 1000$ normalized time units ($\approx 66\ p\sec$). In the strong damping regime the backscattered field saturates at a lower level than that in the intermediate damping regime. This indicates that the reflectivity (SRS_r) is reduced by the EPW damping.

Figure 12(b) shows the backscattered field amplitudes in the weak ($k_3\lambda_{De} = 0.28$) and intermediate ($k_3\lambda_{De} = 0.319$) EPW damping cases. As shown, the backscattered field in the weak damping regime does not evolve to a constant amplitude. Instead, its saturation exhibits time fluctuations that remain constant on the average. In such case, the average backscattering $[\langle SRS_r \rangle = \omega_2 \langle a_2(-450,t) \rangle / \omega_1 a_1(-450,t)]$ is below the backscattering observed in the intermediate EPW damping regime. To understand the effect of the EPW damping on the SRS reflectivity, it is instructive to look at the spatial variation of the fields in steady state.

Figure 13 shows the field amplitudes in steady state, for $k_3\lambda_{De} = 0.4$ (the strong damping regime). The boundary conditions for positive group velocity waves (LASER, EPW and IAW) are set at the left boundary, and for negative group velocity waves (BEMW and BEPW) at the right boundary. The boundary condition of the laser has been set to $a_1(-450,t) = 1$, and all the other boundary conditions to 0.0005 (i.e., an estimated amplitude of the noise level). In steady state, the laser undergoes a small depletion as it propagates through the plasma (from left to right). As explained, the BEMW grows from its boundary condition (right) as it propagates through the plasma with a negative group velocity. The EPW, which relative to the electromagnetic waves is approximately stationary, grows locally according to the amplitudes of the LASER and the BEMW. The LDI daughters are not visible in the figure, because in the strong EPW damping regime LDI is not excited at all.

In steady state, considering that LDI is not excited and the laser amplitude is constant, Equations (8) – (10) can be solved exactly to determine the spatial growth rate of the BEMW:

$$\Gamma_s = -\frac{\nu_3}{2} \pm \left(\nu_3 + 4 \frac{\left| G a_1 \right|^2}{\left| \mathrm{v}_{g2} \right|} \right)^{1/2} .$$

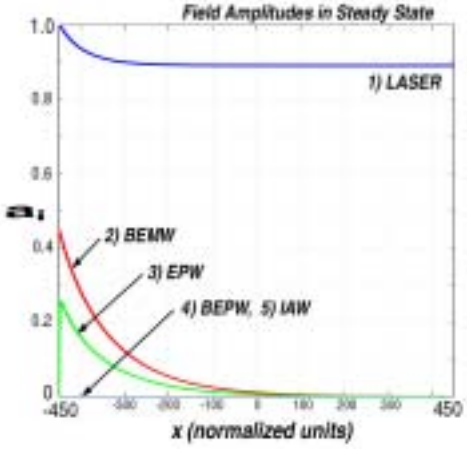

Figure 13: Field amplitudes in steady state, for $k_3 \lambda_{De} = 0.4$ (strong EPW damping).

Where a_1 is constant, the BEMW amplitude in Figure 13 satisfies:

$$a_2(x) = a_2(x = 450) \exp\left[\Gamma_s \cdot (450 - x)\right].$$

The field-amplitudes in steady state for $k_3 \lambda_{De} = 0.319$ (intermediate EPW damping) are illustrated in Figure 14. With the same boundary conditions considered before, we now find that LDI is excited in localized region near the left boundary (where the laser enters the plasma). In $-100 < x < 450$ the amplitude of the EPW (a_3) is not large enough to excite LDI, therefore only SRS is observable. In $-180 < x < -100$ the amplitude of the electron plasma wave is above the LDI threshold condition $\sqrt{\nu_4 \nu_5} \approx 0.132$, therefore LDI is excited. However, LDI is not strong enough to modify the spatial behavior of SRS. In $-448 < x < -180$, after a sharp transition at $x \approx -180$, the nonlinear interaction between SRS and LDI occurs. In such region LDI has a strong effect on the evolution of SRS. Finally, a transition boundary layer exists in $-450 < x < -448$. This boundary layer is shown in detail in Figure 13(b).

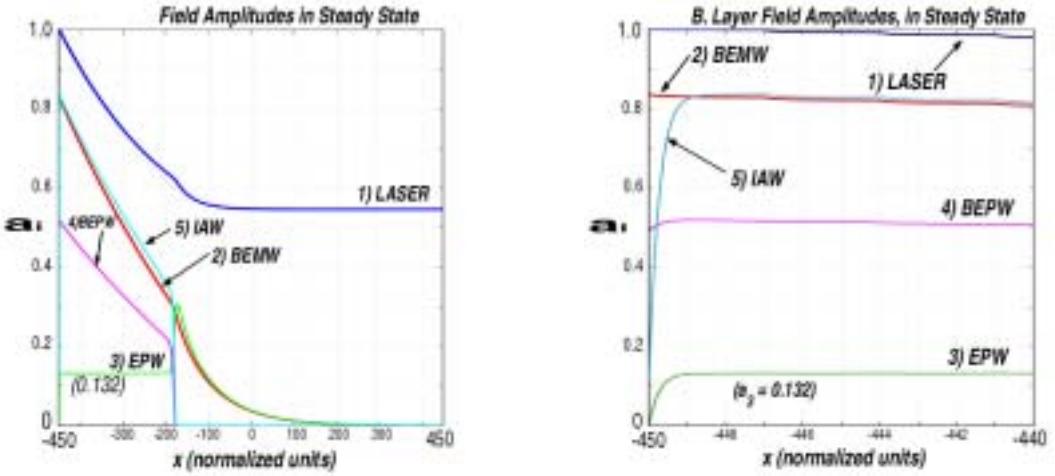

Figure 14: Field amplitudes in steady state, for $k_3\lambda_{De} = 0.319$ (intermediate EPW damping).

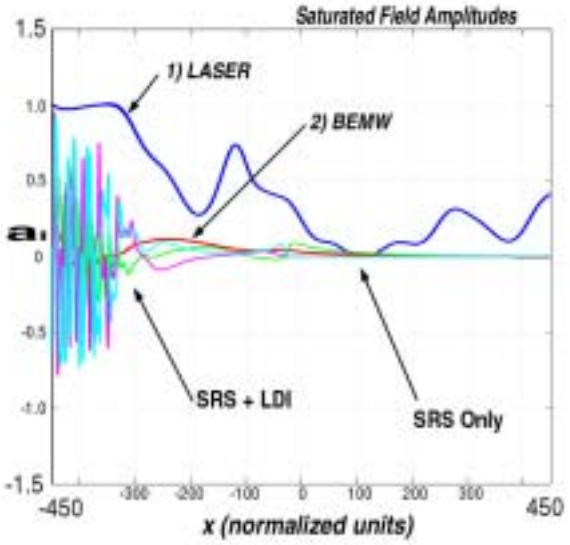

Figure 15: Field amplitudes in saturated state, for $k_3\lambda_{De} = 0.28$ (weak EPW damping).

In the region where LDI is observed to modify SRS, $-448 < x < -180$, the amplitude of the EPW is found to be essentially constant, slightly above the LDI threshold for convective instability $\sqrt{\nu_4\nu_5} \approx 0.132$. This threshold determines the balance between SRS (which tends to increase a_3) and LDI (which effectively damps a_3). This observation is found consistently in numeric simulations with other plasma parameters, corresponding to the intermediate EPW damping regime.

We find that the excitation of LDI reduces the SRS reflectivity. Near the boundary where the laser enters the plasma LDI forces down the amplitude of the EPW (to the LDI threshold). This reduction of a_3 weakens the nonlinear interaction in SRS [a_3a_2 and a_3a_1 in Equations (8) and (9)], thus reducing the amplitude of the SRS backscattering.

Figure 15 illustrates the saturation in the weak-damping regime. Since no definitive steady state occurs (the amplitudes are only constant on the average), we only show the field amplitudes at an arbitrary moment in the saturated state.

Again, the excitation of LDI is localized in a narrow region near the left boundary. In this region, the waves in LDI show incoherent fluctuations in space and time. Figure 16 (a) shows in detail the space-time fluctuations of the EPW (a_3), and Figure 16 (b) its correlation function. The wave de-phasing associated to the incoherent fluctuations observed in the weak-damping regime produce an appreciable reduction of the SRS backscattering (Figure 17).

Figure 17 shows the SRS reflectivity for the different parameters in Table 2. For comparison, the SRS reflectivity without the coupling to LDI [solution of Equations (8)–(10) with $a_4 a_5 = 0$] is also shown. We find that the excitation of LDI reduces the SRS reflectivity. This becomes more significant in the weak-damping regime, where the space-time incoherence in LDI introduces a strong wave de-phasing.

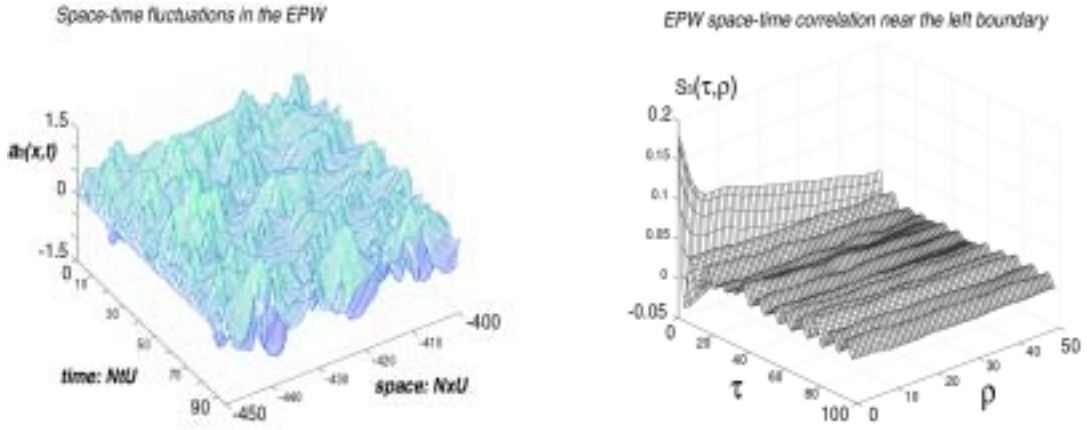

Figure 16: Detailed view of the incoherent space-time fluctuations, and the correlation function, of the EPW amplitude, for $k_3\lambda_{De} = 0.28$ (weak EPW damping).

We have also investigated the effect of ion acoustic wave damping and laser intensity, finding an SRS reflectivity that varies in a manner similar to experiments.[20] However, our calculations fail to quantitatively predict the (much lower) experimental SRS reflectivity. Recent experiments[2] have shown that coupling of SRS to LDI also exhibits LDI cascades. We have extended the coupled-mode equations model to include the effects of possible LDI cascades, and in addition, we have also studied possible cascades of SRS. While LDI cascades reduce the effect of LDI on SRS, and thus slightly increase the SRS reflectivity, SRS cascades are more effective in reducing the SRS reflectivity.[3] While these extended models show interesting dynamics in the coupling of SRS and LDI, they still fail to quantitatively predict the observed reflectivity. Although the coupled-mode equations give a simple model for understanding the coupling of SRS to LDI and their cascades, they do not account for other nonlinear effects – such as trapping of electrons in EPWs (see previous section) and filamentation – which may be critical in determining the observed saturated reflectivity.

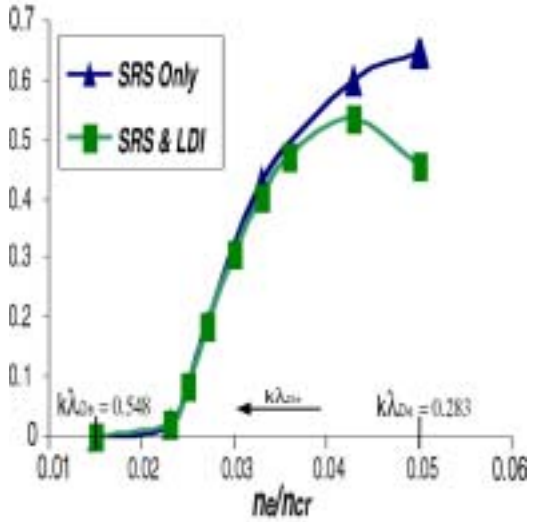

Figure 17: SRS reflectivity for SRS only, and SRS with LDI.

3. New Code and Results on LHCD and ECCD Synergism With the Bootstrap Current

Sponsors
Department of Energy (DoE) Contract DE-FG02-91ER-54109

Project Staff
J. Decker, Dr. Y. Peysson, Professor A. Bers, and Dr. A. K. Ram

Many recent scenarios for high-performance steady-state tokamak operation rely on a high-bootstrap fraction current generation supplemented and controlled by radio-frequency current drive (RFCD).[21] Therefore, a self-consistent calculation of the bootstrap current in the presence of RFCD is necessary to predict accurately the total current generated, including possible synergistic effects. Such a theory has been developed and a code has been written that showed the existence of a positive synergistic current for both the case of lower-hybrid current drive (LHCD) and electron-cyclotron current drive (ECCD).[4,22] Since then, a new and improved code based on the same model has been developed. Thanks to a new, implicit, and more accurate treatment of the boundary between trapped and passing electrons in momentum space, the new code calculates the steady-state current generation self-consistently with the bootstrap current in a much shorter time. This fast code allows an extensive study of the synergism between RFCD and the bootstrap current, and has led to a new understanding of the physical mechanisms responsible for the synergistic current.

The code FP2DYP has been written by Y. Peysson in MATLAB, based on the code FASTFP developed by M. Shoucri and I. Shkarofsky.[23] It solves the steady-state relativistic Fokker-Planck equation with quasilinear diffusion due to lower hybrid waves and electron cyclotron waves. According to the model developed by S. Schultz,[4,22] we extended this code to include the effects of radial drifts due to the magnetic field gradient and curvature, thus taking into account neoclassical effects including the bootstrap current. The model is developed in the low collisionality regime (banana regime), where the electrons trapped in the low magnetic field side can be reflected many times (bounce motion) before undergoing a collision, their guiding center thus following a so-called banana orbit. The trapping occurs because these electrons have insufficient parallel energy to counter the magnetic mirror force in the inhomogeneous magnetic field ($\vec{B}_T + \vec{B}_P$); their motion entails a momentum pitch angle

$$\frac{p_{//}}{p} = \xi < \xi_{0T} \tag{13}$$

where $\xi_{0T} = \sqrt{2\varepsilon/(1+\varepsilon)}$ and $\varepsilon = r/R$. Because of this fast bounce motion (compared to collision and quasilinear times), the zero-order electron distribution function in the trapped momentum space is essentially symmetric in $p_{//}$; this has to be imposed in the Fokker-Planck code. Instead of forcing the symmetrization at each time step, as done in [4,22], we accounted for it implicitly by solving the Fokker-Planck equation only in one half ($p_{//} > 0$) of the trapped momentum space. The conservation of particle fluxes in the velocity space requires a specific treatment at the boundary

[21] P. T. Bonoli et al., "Modelling of Advanced Tokamak Scenarios With LHCD in Alcator C-Mod," *Nucl. Fusion* **40**, 1251 (2000).
[22] S. D. Schultz, A. Bers, and A. K. Ram, "Plasma Electrodynamics and Applications: Section 1 – Current Drive in the Presence of Bootstrap Current in Tokamaks," *Progress Report No. 142,* MIT Research Laboratory of Electronics, Cambridge, 2000 (http://rleweb.mit.edu/Publications/pr142/bers142.pdf).
[23] M. Shoucri and I. Shkarofsky, "A Fast 2D- Fokker-Planck Solver with Synergetic Effect," *Comp. Phys. Comm.* **82**, 287 (1994).

between trapped and passing electrons; the different domains in the momentum space and the flux conservation equations are displayed in Figure 18.

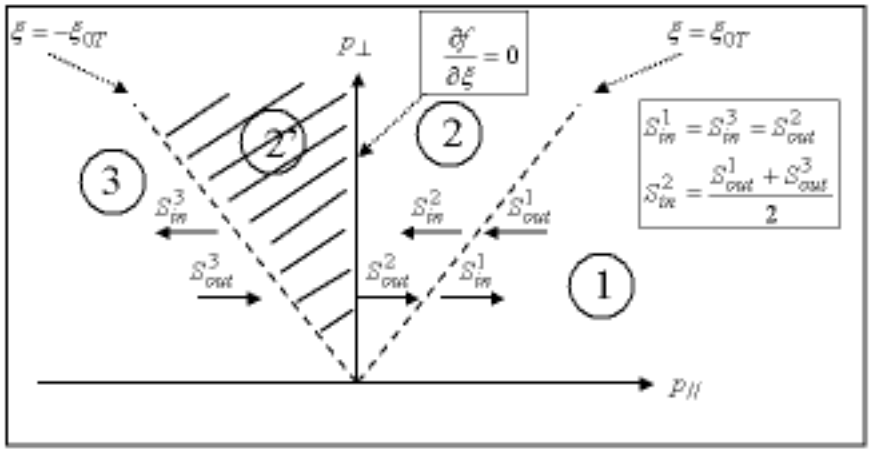

Figure 18: The momentum space is divided in: (1) co-passing domain, (2) and (2') trapped domain, (3) counter-passing domain. The equations for flux conservation at the trapped-passing boundaries ($\xi = \pm\xi_{0T}$) and at $p_{//} = 0$ are displayed.

In particular, the fluxes between the counter-passing domain and the trapped domain in momentum space must be taken into account by connecting the regions (2) and (3), as shown in Figure 18. This leads to a 15-diagonal discretization scheme instead of the usual 9-diagonal (center point plus eight neighboring points) discretization scheme. The symmetrization is now treated in a completely implicit manner, which allows the use of large time steps in the solution of the Fokker-Planck equation, thus significantly reducing the calculation time.

Among other improvements with respect to the previous code, we can note the use of a modified discretization process, where the distribution function is calculated on the half-grid and the fluxes on the main grid. This allows a direct simplification of the external boundary condition on the fluxes, due to the properties of the divergence operator in spherical geometry (at $p = 0$ and $\xi = \pm 1$). Moreover, our new code is structurally three-dimensional, in the sense that the (p, ξ) grid can be set independently of the local temperature and density, so that calculations at different flux-surfaces are self-consistent. This condition is particularly important for the calculation of the radial derivative of the distribution function, which is needed for the calculation of the bootstrap current.[4,22] This treatment, which requires a proper normalization of the distribution in the calculation of collision operators,[24] also allows for the eventual further inclusion of radial transport.

The synergism between LHCD and the bootstrap current has been studied in the specific case of an Alcator C-Mod advanced operation scenario.[21] At the radial position $r = 0.15\,\mathrm{m}$ (where a large LH driven current is needed) with realistic LH spectrum parameters ($\mathrm{v}_1 = 3.5\,\mathrm{v}_{Te}$, $\mathrm{v}_2 = 6.0\,\mathrm{v}_{Te}$, $D_{LH} = 1.0\,\nu_e\,p_{Te}^2$), the current densities calculated by our code are $J_{//}^{LH} = 10.9$ MA/m^2 (LH driven

[24] I. P. Shkarofsky and M. M. Shoucri, "Modelling of Lower-Hybrid Current Drive in the Presence of Spatial Radial Diffusion," *Nucl. Fusion,* **37**, 539 (1997).

current neglecting the bootstrap current), $J_{//}^{BS} = 3.7$ MA/m^2 (bootstrap current in the absence of LHCD) and $J_{//}^{TOT} = 15.2$ MA/m^2 (total current calculated self-consistently). Thus,

$$J_{//}^{TOT} - J_{//}^{LH} - J_{//}^{BS} \equiv J_{//}^{S} = 0.6 \text{ MA/m}^2 \tag{14}$$

is the synergistic fraction. In this particular case, it represents only a small fraction (5%) of the driven current. The rather small level of synergism between LHCD and the bootstrap current can be understood kinetically: the bootstrap current is generated by electrons that are near the trapped-passing boundary, with large perpendicular momentum, while LHCD is driven mostly with electrons which have a high parallel momentum and therefore are well-passing. The populations involved with the respective processes being well separated (in momentum space), the synergism is limited to a small fraction of the current. The physical mechanism for this synergism can be described in one dimension. In fact, the electron distribution associated with the bootstrap current presents a tail that brings more electrons to the region ($v = v_1$), thus enhancing the level of the LH plateau which is responsible for the LH current. Another way to explain the synergism consists of saying that the tail of the first-order drift-kinetic distribution function, which generates the bootstrap current, is enhanced by LHCD as well and therefore a plateau is raised in this distribution.[4,22] The two interpretations are equivalent. A simple analytical calculation performed in the Lorentz limit ($Z_i \to \infty$) and based on the 1-D interpretation has been carried out in [4,22]; it gives the following expression for the synergistic fraction:

$$\frac{J_{//}^{S}}{J_{//}^{LH}} \approx \frac{J_{//}^{BS}}{3en_e v_{Te}} \left(\frac{v_1}{v_{Te}} \right)^3 . \tag{15}$$

This simple formula predicts that the synergism should increase with the bootstrap current, which is intuitively expected, and with the cubic power of the lower bound of the LH spectrum $(v_1/v_{Te})^3$. This dependence upon v_1 comes from the fact that the tail of the electron distribution associated with the bootstrap current decreases with momentum as $(v_1/v_{Te})^3 \exp\left[-(p/p_{Te})^2/(1+\gamma)\right]$. The analytical formula (15), based on the Lorentz model and the 1-D interpretation of the synergism, has been tested extensively for various LH and plasma parameters. It was found to scale remarkably well in all cases, including for scenarios with high bootstrap current. However, the current obtained from the analytical prediction of (15) is constantly larger than the current calculated with the code by a factor of 2, which can be attributed in part to the neglected 2-D effects, and in part to the Lorentz approximation. The synergistic fraction can be expected to be more significant (up to 15%) if the LH power is absorbed at a location where the bootstrap current is large (where the pressure gradient is high, for example in dense, hot plasmas or at the location of internal transport barriers).

While LHCD is mostly a 1-D process (in momentum space), ECCD is associated with a quasilinear diffusion that occurs mostly in the perpendicular direction. Moreover, it concerns only electrons that have a significant perpendicular energy and which can eventually be close to or within the trapped region, where the bootstrap current is generated. Therefore, the synergism between and the bootstrap current and ECCD is intrinsically 2-D, and can be expected to be sensibly larger than in the case of LHCD. We considered the hypothetical case of second harmonic, X-mode ECCD in Alcator C-Mod at the radial position $r = 0.15$ m. By exploring the range of EC parameters extensively, the maximum EC driven current at this location was found to occur with the launching parameters $N_{//} = 0.29$ and $\omega = 2\Omega_{ce}/0.97$, which generate a current density $J_{//}^{EC} = 1.8$

MA/m^2 with $D_{EC} = 0.4 \nu_e p_{Te}^2$. The total current density resulting from the self-consistent calculation was found to be $J_{//}^{TOT} = 6.1$ MA/m^2. Therefore, the synergistic current is

$$J_{//}^{S} \equiv J_{//}^{TOT} - J_{//}^{EC} - J_{//}^{BS} = 0.6 \text{ MA/m}^2 \tag{16}$$

which in this case represents a large fraction $J_{//}^{S} / \left(J_{//}^{TOT} - J_{//}^{BS} \right) = 25\%$ of the driven current. However, the total driven current remains small in this particular case and would not be sufficient by itself for the scenarios described in [21].

A first attempt to explain the synergism between ECCD and the bootstrap current was to simply consider the overall increase of the temperature due to ECCD that would modify the pressure profile and therefore increase the bootstrap current.[4,22] The increase in temperature can be calculated from the distribution function, using

$$\Delta T = \frac{1}{3 n_e} \int \frac{1}{2} m_e \mathrm{v}^2 \left(f - f_M \right) d^3 p \tag{17}$$

where f_M is the Maxwellian distribution function at the initial temperature, taken as $T = 2.1$ keV. In the particular case presented above, we found an increase in temperature of $\Delta T = 0.10$ keV, which leads only to a slight increase in the bootstrap current density ($J_{//}^{\Delta T} = 0.05$ MA/m^2); this represents less than 10% of the synergism found with the code. Clearly, a simple increase in temperature cannot explain the synergism, which must be related to more detailed kinetic effects. A 2-D representation of the distribution function is required in order to understand the mechanism of the synergism.

Figure 19 shows the first-order electron distribution f_1, which describes the effects of radial drifts including the bootstrap current. It shows that these electrons are subject to EC diffusion as well, resulting in a change in the resistivity associated with these electrons and an increase in the bootstrap current. The synergistic effect is significant in this case because the EC diffusion occurs in a region of velocity space where f_1 is large. The corresponding electrons are suprathermal ($p / p_{Te} > 3$) and barely passing ($\xi \geq \xi_{0T}$); they are not very collisional and drive an important part of the bootstrap current. Increasing their perpendicular energy with EC diffusion reduces further their resistivity, thus enhancing the bootstrap current.

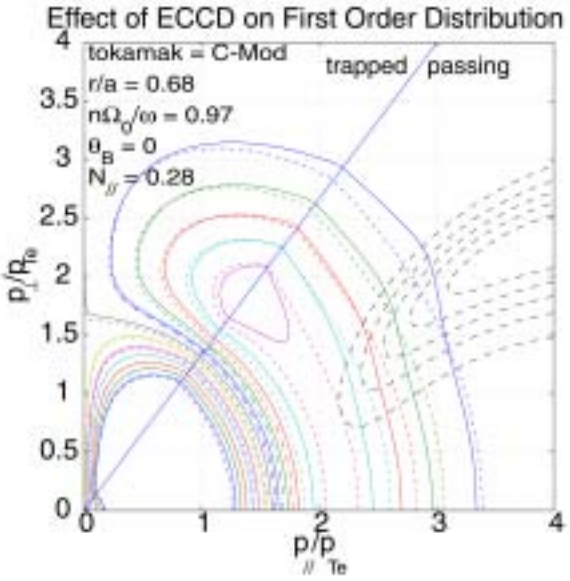

Figure 19: 2-D contour plot of the first-order drift-kinetic distribution function f_1. The dotted line is f_{1M}, obtained from a zero-order Maxwellian distribution (no ECCD). The solid line describes the distribution when ECCD is present. The black dashed lines are a contour plot of the EC diffusion coefficient.

4. Chaotic Dynamics in Two Electrostatic Waves Propagating Obliquely to $\vec{B}_0$

Sponsors
Department of Energy (DoE)/National Science Foundation (NSF) Contract DE-FG02-99ER-54555

Project Staff
D. J. Strozzi, Dr. A. K. Ram, and Professor A. Bers

The motion of a charged particle in traveling electrostatic waves and a uniform magnetic field $\vec{B}_0$ is a rich problem in nonlinear dynamics and in the understanding of the physics of nonlinear wave-particle interactions. Such wave-particle interactions are important in space plasmas and in RF heating/current drive of plasmas in fusion experiments.

We have extended earlier work done by this group on the energization of ions by multiple electrostatic waves to include finite wavenumbers along the magnetic field. Ram et al.[5] have previously analyzed the motion of an ion in the presence of two electrostatic waves propagating perpendicular to $\vec{B}_0$. They found that the region of phase space where the motion is stochastic is roughly given by the same conditions found by Karney[25] for one wave. However, coherent motion leading to ion energization over a long time scale was also observed in the special case where the wave frequencies differed by an integer multiple of the cyclotron frequency. For certain initial conditions, a particle with energy well below the stochastic threshold can be accelerated into the stochastic region.

The latest analysis[26] includes waves with wavevectors $\vec{k}_i$ not strictly perpendicular to $\vec{B}_0 = B_0\hat{z}$. The main difference between the present and previous studies is that now the effective wave frequencies must be Doppler-shifted by $k_{iz}\, v_z$, and their difference shifted by $(k_{1z} - k_{2z})\, v_z$. As the wave frequency difference now depends on time, via v_z, the ions are not strictly in resonance with the waves, and the coherent energization of ions decreases as $k_{1z} - k_{2z}$ grows. The coherent motion in z is simply related to the Larmor radius via a new, approximate constant of the motion.

The nondimensional equations of motion for a particle in a magnetic field $\vec{B}_0 = B_0\hat{z}$ and two electrostatic waves are

$$\ddot{\vec{x}} = \vec{\mathrm{v}} \times \vec{B} + \sum_{i=1}^{2} \vec{\varepsilon}_i \sin(\vec{k}_i \cdot \vec{x} - \omega_i t), \quad \vec{\varepsilon}_i = \varepsilon_i \hat{k}_i \tag{18}$$

where ε_i is the amplitude of the i^{th} wave and time has been normalized to the ion cyclotron frequency $\Omega = q\, B_0/\mathrm{m}$. If we restrict attention to two waves propagating in the x-z plane and work in a reference frame in which the constant canonical y-momentum is zero, we have (with an implied sum over i)

$$\ddot{x} + x = \varepsilon_{ix} \sin(\vec{k}_i \cdot \vec{x} - \omega_i t), \quad \ddot{z} = \varepsilon_{iz} \sin(\vec{k}_i \cdot \vec{x} - \omega_i t). \tag{19}$$

We perform a multiple timescale analysis of these equations to study the coherent evolution. Let δ order the timescales $T_i = \delta^i t$. We also order $\varepsilon_i \sim \omega_i^{-1} \sim \delta$. The zeroth-order solution is

[25] C. F. F. Karney, "Stochastic ion heating by a lower hybrid wave," *Phys. Fluids* **21**,1584 (1978).
[26] D. J. Strozzi, A. K. Ram, and A. Bers, "Stochastic Particle Motion due to Multiple Electrostatic Waves," poster presented at the American Physical Society Division of Plasma Physics Annual Meeting, Long Beach, California, October 29 – November 2, 2001.

$$x_0 = r\sin(T_0 + \varphi), \quad z_0 = \mathrm{v}_z T_0 + C_z \tag{20}$$

where r is the Larmor radius and measures the perpendicular kinetic energy [$r^2 = (v_x^2 + v_y^2) / \Omega$], and φ is a slowly-varying phase. If we assume that no ν_i is an integer (i.e., the wave frequencies are not integer multiples of Ω), then there are no large (e.g., resonant) driving terms to first order. We define the Doppler-shifted frequency difference by

$$N \equiv \omega_1 - \omega_2 - (k_{1z} - k_{2z})\mathrm{v}_z . \tag{21}$$

The second-order equation of motion for x contains resonant and near-resonant terms:

$$\begin{aligned} \ddot{x}_2 + x_2 = &-2\frac{\partial r}{\partial T_2}\cos(T_0 + \varphi) + 2r\frac{\partial \varphi}{\partial T_2}\sin(T_0 + \varphi) \\ &+ A_{ijlm}\sin[(l - m + N_{ij})T_0 + \varphi_{ijlm}] \end{aligned} \tag{22}$$

Let

$$\eta \equiv N - N_0 = (k_{1z} - k_{2z})(\mathrm{v}_z - \mathrm{v}_{z0}) \tag{23}$$

(zero subscripts denote initial values). We consider the case where N_0 is an integer, so that η measures the departure of the system from exact resonance. If v_z changes slowly enough, η remains small enough for near-resonant terms on the right-hand side (RHS) ($i \neq j$) to drive large-amplitude x_2 motion. We set the entire RHS to zero in order to keep x_2 small.

This gives the slow evolution of r and φ, which can be put in Hamiltonian form:

$$I \equiv \frac{r^2}{2}, \quad H \equiv -S_1[I] - S_2[I]\cos[N_0\varphi - \eta T_0 + (k_{1z} - k_{2z})C_z] \tag{24}$$

$$\frac{d\varphi}{dt} = \frac{\partial H}{\partial I}, \quad \frac{dI}{dt} = -\frac{\partial H}{\partial \varphi} \tag{25}$$

$$S_1 = \frac{1}{4}\sum_{m=-\infty}^{\infty}\left(\frac{\varepsilon_{1x}^2 J_{1m}^2 + \varepsilon_{2x}^2 J_{2m-N_0}^2}{1-(m-\omega_{1z})^2} - \frac{\varepsilon_{1z}^2 J_{1m}^2 + \varepsilon_{2z}^2 J_{2m-N_0}^2}{(m-\omega_{1z})^2}\right) \tag{26}$$

$$S_2 = \frac{1}{2}\sum_m\left(\frac{\varepsilon_{1x}\varepsilon_{2x}}{1-(m-\omega_{1z})^2} - \frac{\varepsilon_{1z}\varepsilon_{2z}}{(m-\omega_{1z})^2}\right)J_{1m}J_{2m-N_0} \tag{27}$$

where $J_{im} = J_m(k_{ix}\sqrt{2I})$, J = Bessel function of first kind.

Due to the sinusoidal form of H, we can put bounds on H as a function of r:

$$H_- \leq H \leq H_+, \quad \text{where} \quad H_\pm \equiv -S_1 \pm |S_2| \tag{28}$$

In the case of perpendicular propagation, $\eta = 0$, H has no explicit time dependence, and, therefore, H is a constant of the motion. For a given initial r and φ, we determine the turning points of H (that

is, the location where H reaches one of the bounding $H_{\pm}$ curves). If this happens before the chaotic regime, the particle's orbit will remain coherent; otherwise its motion will become chaotic. Oblique propagation complicates this picture. Unlike the perpendicular case, the Hamiltonian now depends explicitly on the time via ηT_0, and η itself slowly evolves with time as v_z does. Since H now has an explicit time dependence it is no longer a constant of the motion. H must still satisfy the bounds, but given an initial H we cannot predict where the ion's turning points are. This makes it difficult to put an approximate bound on the r motion for given initial conditions.

The second-order equation for z_2 can contain sinusoidal driving terms of any frequency, but it cannot contain constant driving terms ($\ddot{z}_2 = c \rightarrow z_2 \sim t^2$, which grows faster than $z_0 \sim t$). Eliminating these terms gives the slow evolution of v_z , which is closely linked to r through a new, approximate (to second order) constant of the motion, K_2:

$$K_2 = v_z - \frac{k_{1z} - k_{2z}}{N_0} I \tag{29}$$

We note that when $k_{1z} = k_{2z}$, there is no coherent z-motion, and $\eta = 0$. However, modest values of $k_{1z} - k_{2z}$ cause enough z acceleration to significantly reduce the coherent motion.

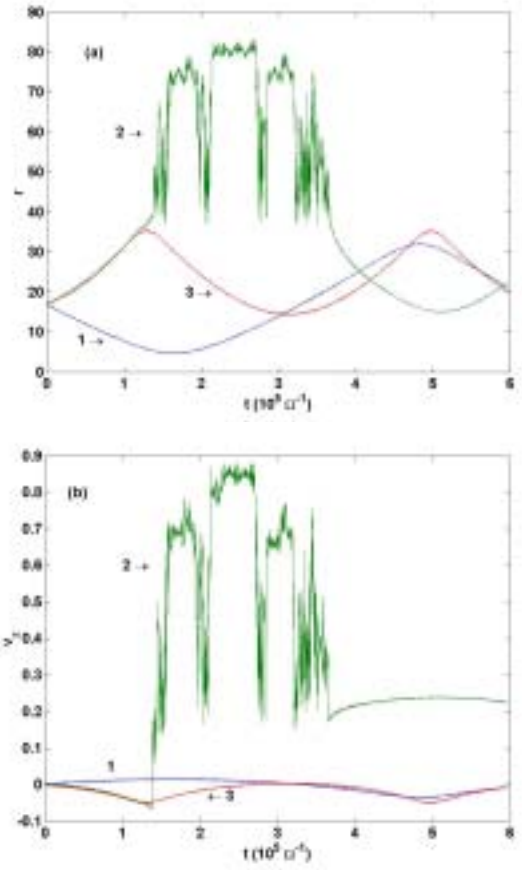

Figure 20: (a) r vs. t and (b) v_z vs. t for k_{1z} = 0.01, k_{2z} = 0.0101 using parameters relevant to lower-hybrid waves on Alcator C-mod: ω_1 = 40.47, $\omega_2 = \omega_1 - 1$, $k_{1x} = k_{2x}$ = 1, $\varepsilon_1 = \varepsilon_2$ = 3.2. All orbits start with r = 17, initial φ's are -0.6π, 0.2π, and 0.3π for orbits 1, 2, and 3, respectively.

Figure 20 displays the slow, coherent motion in both r and z for a parallel wavenumber difference of 10^{-4} ($k_{1z} = 0.01$, $k_{2z} = 0.0101$) and $N_0 = 1$. Note that below the stochastic region the evolution of v_z and r is in opposite directions to each other, as is required for K_2 to remain constant.

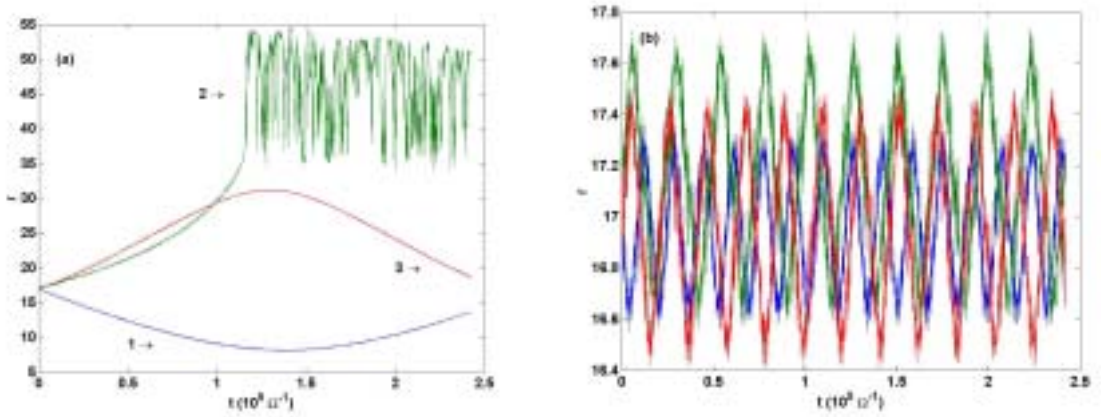

Figure 21: r vs. t for (a) $k_{1z} = 1$, $k_{2z} = 1.0001$ and (b) $k_{1z} = 0.01$, $k_{2z} = 0$ using same parameters and initial conditions as Figure 20.

Figure 21(a) is for larger values of k_z while maintaining the same difference between k_z's as in Figure 20. The behavior is similar to that observed before, consistent with our analysis (where only the difference in k_z and not the absolute size enters). When we increase the difference in k_z to 0.01, the amplitude of the coherent motion is greatly reduced as seen in Figure 21(b).

Figure 22 shows the temporal evolution of K_2 for the three orbits of Figure 20. There is no coherent drift in K_2, although there are high-frequency, low-amplitude fluctuations which appear in the higher-order and which are not included in the zeroth-order motion (r, φ, v_z).

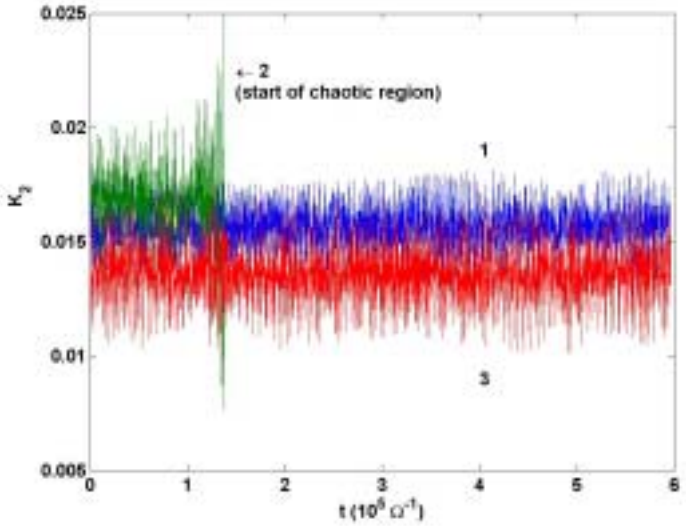

Figure 22: Approximate constant K_2 using data from Figure 20.

We demonstrate the Hamiltonian nature of the perpendicular motion in Figure 23. The smooth curves are H_+ and H_-, which bound H [Equation (28)]. The three jagged curves are the numerical values of H using the three orbits in Figure 20. H is not conserved due to the finite difference in parallel wavenumbers. If $k_{1z} = k_{2z}$, particles 2 and 3 would both pass the inverted "hump" in H_+ and reach the chaotic regime at $r \approx 40$, while particle 1 would not. The time dependence in H causes particle 3 to not make it past the hump. Notice that none of the particles has a turning point when H touches H_+. In particular, particle 2 continues to grow in r until it passes the hump even after it hits H_+ and goes into the chaotic r-space.

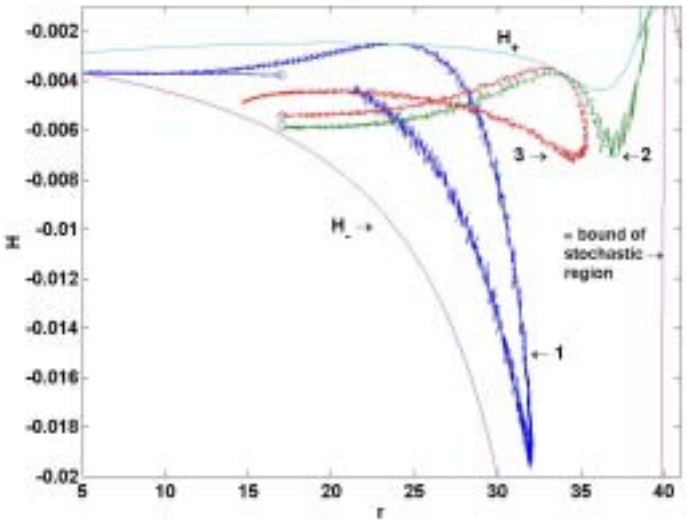

Figure 23: Plot of numerically-calculated Hamiltonian H from Equations (24)–(27), as well as analytic bounds $H_\pm$ from Equation (28), showing the difficulty in predicting whether a particle will reach the chaotic region when the wavenumbers are oblique. Circles indicate initial conditions.

5. Energization of Ions by Spatially Localized Fields

Sponsors
Department of Energy (DoE)/National Science Foundation (NSF) Contract DE-FG02-99ER-54555 and National Science Foundation (NSF) Contract ATM 98-06328.

Project Staff
Dr. A. K. Ram and Professor A. Bers

There are two observations that are particularly ubiquitous in the auroral ionospheric plasmas: intense lower hybrid fields in density depleted regions localized transverse to the geomagnetic field, and transverse energization of ions emanating from the fields in the density depleted regions.[27] Theoretical and computational studies directed towards understanding the generation of fields in density cavities and their interaction with ionospheric ions were reported on in the last progress report.[28] In a density gradient, spatially localized intense electric fields can be generated in regions where plasma resonances exist. These resonances occur where the wave frequency matches the local lower hybrid frequency or the upper hybrid frequency. The singularity in the amplitude of the wave at these spatial locations is logarithmic.

We now report our studies on the interaction of ions with these spatially localized fields in order to understand the transverse energization of ions that is observed in the auroral ionosphere.

We consider an ion in a uniform magnetic field $\vec{B} = B_0 \hat{z}$ interacting with a radially localized electrostatic structure:

$$\vec{E}(r,\theta,t) = E_0\, e^{-\beta(r-a)^2} \sum_n \sin\,(k_n r + m_n \theta - \omega_n t + \phi n_n)\hat{r} \tag{30}$$

where r and θ are the radial and azimuthal coordinates, respectively, E_0 is the electric field amplitude, a is the radius of the cavity (or the radial location where the localized field is centered), and k_n, m_n, ω_n, and ϕ_n are the radial wavevector, azimuthal mode number (integer), angular frequency, and phase of the n-th wave, respectively. Figure 24 shows the interaction region (thick circle) in which the field is localized. The half-width of the interaction region is $\approx 1/\sqrt{\beta}$.

The equations of motion of an ion interacting with the radial field (30) are given by:

$$\frac{dr}{dt} = \mathrm{v}_r \tag{31}$$

$$\frac{d\theta}{dt} = \frac{\mathrm{v}_\theta}{r} \tag{32}$$

[27] K. A. Lynch, R. L. Arnoldy, P. M. Kintner, P. Schuck, J. W. Bonnell, and V. Coffey, "Auroral Ion Acceleration From Lower Hybrid Solitary Structures: A Summary of Sounding Rocket Observations," *J. Geophys. Res.*, **104**, 28515 (1999).
[28] A. Salcedo, M.-J. Wu, A. K. Ram, and A. Bers, "Plasma Electrodynamics and Applications: Section 3 – Modes in Density Depleted Waveguides in Space Plasmas," and A. Bers, A. K. Ram, M.-J. Wu, and A. Salcedo, "Plasma Electrodynamics and Applications: Section 4 – Variational Principle for Modes With Resonant Absorption," *Progress Report No. 143,* MIT Research Laboratory of Electronics, Cambridge, 2001 (http://rleweb.mit.edu/Publications/pr143/Chapter-19-web.pdf).

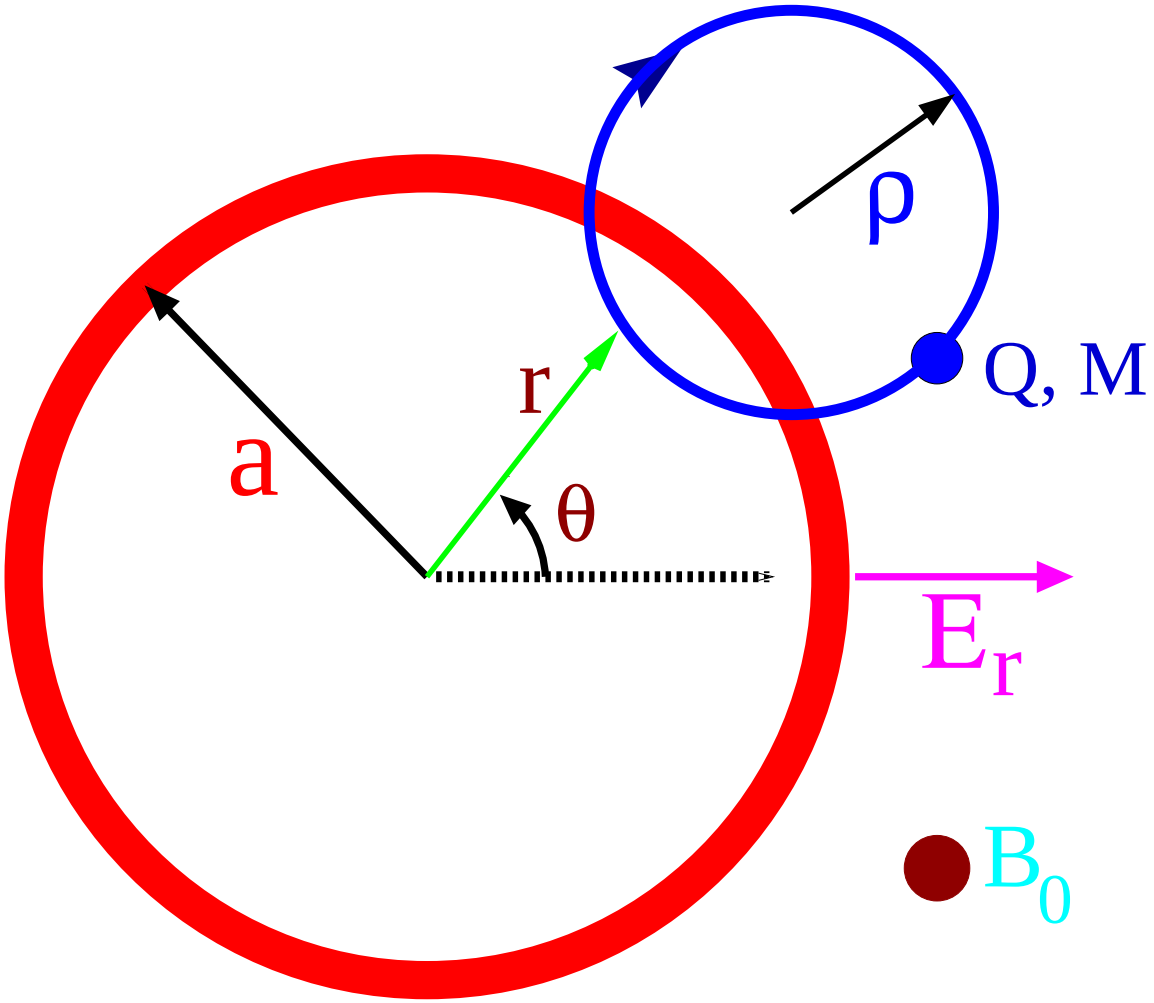

Figure 24: A pictorial representation, in *x*-*y* plane, of an ion of charge *Q*, mass *M*, and Larmor radius ρ, interacting with a cylindrical density depletion of radius *a*. The radial electric field E_r is spatially localized and is qualitatively indicated by the thick circle. The ambient geomagnetic field is out of the plane of the paper. The cylindrical coordinates are indicated by *r* and θ.

$$\frac{dv_r}{dt} = v_\theta\left(\Omega + \frac{v_\theta}{r}\right) + \frac{QE_r}{M} \tag{33}$$

$$\frac{dv_\theta}{dt} = -v_r\left(\Omega + \frac{v_\theta}{r}\right) \tag{34}$$

where v_r and v_θ are the radial and azimuthal velocities of the ion, respectively, *M* and *Q* are the mass and charge of the ion, respectively, E_r is the coefficient of $\hat{r}$ in the right hand side of (30), and $\Omega = QB_0/M$ is the ion cyclotron frequency.

The equations of motion given above have been integrated numerically for the following parameters: B_0 = 0.36 Gauss, *a* =10 m, *f* = 5 kHz, and *T* = 0.33 eV. (*T* is the ion temperature.)

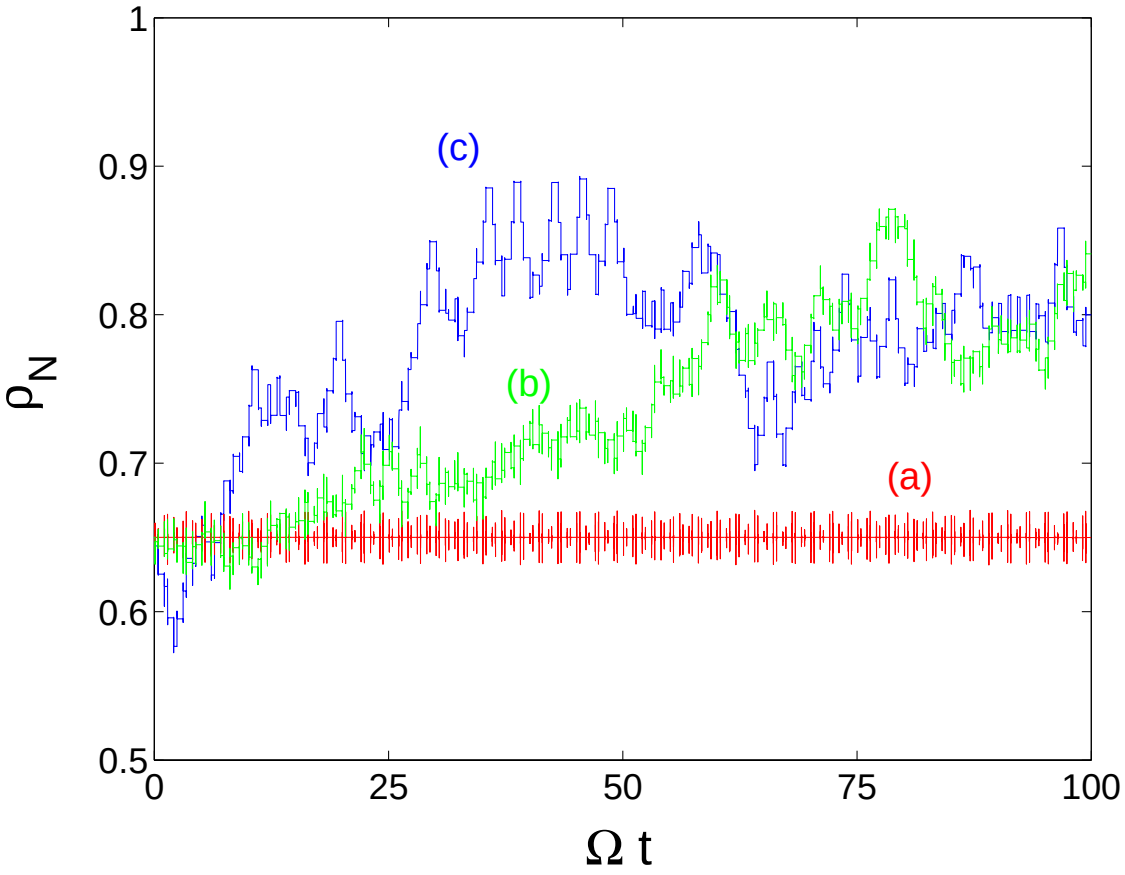

Figure 25: The normalized ion Larmor radius as a function of time for three cases: (a) Δr = 0.4 m, (b) Δr = 0.18 m, and (c) Δr = 0.13 m.

Figure 25 shows the normalized Larmor radius $\rho_N = \rho / a$, where $\rho^2 = \left(v_r^2 + v_\theta^2\right)/\Omega$, for an O^+ ion for three different values of β. Note that $\Delta r = 2 / \sqrt{\beta}$ is a measure of the full width of the region where the electrostatic fields are localized. The three curves in Figure 25 are for (a) Δr = 0.4 m, (b) Δr = 0.18 m, and (c) Δr = 0.13 m. The energization of O^+ depends on the spatial (radial) width of the localized electric field structure. There is a threshold for the width above which the ion energization ceases. For widths below the threshold, the ion motion becomes chaotic. Further analysis of this motion is under progress. Figure 26 shows the ion orbit, in the normalized *x-y* plane, as a function of time for case (c) of Figure 24. The thick circle marked *E* indicates the region where the field is localized.

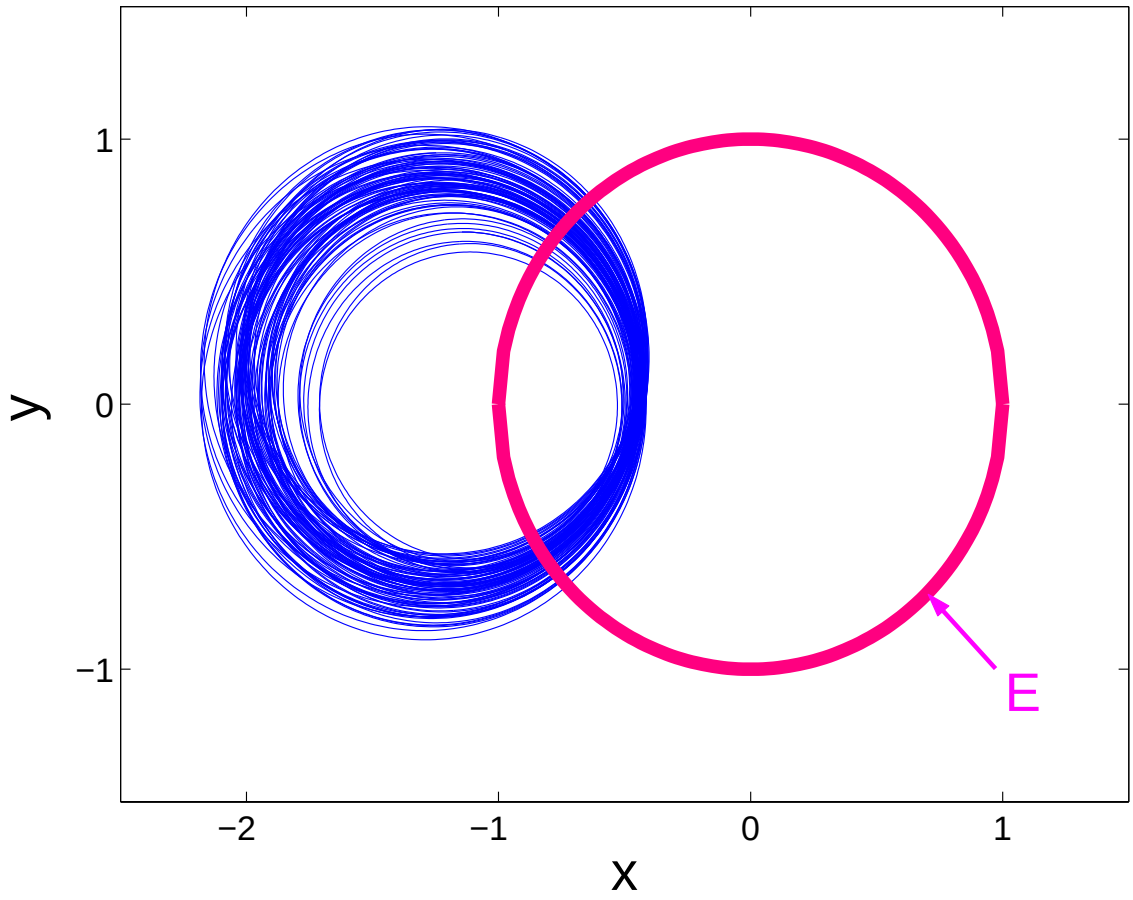

Figure 26: The ion orbit in the *x*-*y* plane for Δr = 0.13 m. Here *x* and *y* are normalized to the radius of the density cavity *a* = 10 m. *E* indicates the region of the localized field.

6. General Proof of Symmetries in Dissipation-Free Mode Conversions and Applications

Sponsors
Department of Energy (DoE) Contract DE-FG02-91ER-54109 and Department of Energy (DoE) /National Spherical Tokamak Experiment (NSTX) Contract DE-FG02-99ER-54521.

Project Staff
Professor A. Bers and Dr. A. K. Ram

We consider linear mode conversions (MC) in a dissipation-free region of the plasma. Outside of this mode conversion region (MCR), the waves are described by their WKB form and have wave energy flows into and out of the MCR. From general properties of wave energy flow conservation and Onsager-like time reversibility on energy flow, we derive symmetry properties that must be satisfied by waves undergoing coupling through mode conversion.[29]

Consider first a one-dimensional (in x) generic propagation situation in an inhomogeneous plasma, with unperturbed (equilibrium) parameters (e.g., density, temperature, and magnetic field) that vary in x, as shown schematically in Figure 27. In the WKB regions to the right and left of the loss-free mode conversion region (LF-MCR), we let the complex field amplitudes of (e.g., forward) waves with energy flow into and out of the LF-MCR be, respectively,

$$a_p \sim \exp(ik_x x - i\omega t) \tag{35}$$

$$b_p \sim \exp(-ik_x x - i\omega t) \tag{36}$$

and normalized so that

$$|a_p|^2 = \text{energy flow density into the LF-MCR} \tag{37}$$

$$|b_p|^2 = \text{energy flow density out of the LF-MCR} \tag{38}$$

[For backward waves, retaining the normalizations in (37) and (38), the signs of the k_x's in (35) and (36) will change.]

On Figure 27, such modes on the left of the LF-MCR have $p = m$ (there can be any number of such modes: m_1, m_2,…), and on the right of the LF-MCR, similarly, $p = n$ (n_1, n_2,…). For a weakly dissipative mode, the total wave energy flow density (electromagnetic plus kinetic) is given, in general, by[30]

$$\left\langle s_x \right\rangle_p = \left[\frac{1}{2} \mathrm{Re}(\vec{E} \times \vec{H}^*)_x - \frac{\varepsilon_0}{4} \omega \frac{\partial \chi^H_{\alpha\beta}}{\partial k_x} E_\alpha E^*_\beta \right]_p , \tag{39}$$

[29] A. Bers and A. K. Ram, "General Proof of Symmetries in Mode Conversions," *Bull. Amer. Phys. Soc.,* **46 (11)**, 19 (2001).
[30] A. Bers, Section 8.5, "General Properties of Dispersive Media," in *Waves in Anisotropic Plasmas,* W. P. Allis, S. J. Buchsbaum, and A. Bers (M.I.T. Press, Cambridge, Massachusetts, 1963, and the University of Tokyo Press, International Edition, Tokyo, Japan, 1964); A. Bers, "Linear Waves and Instabilities," in *Plasma Physics – Les Houches 1972,* eds. C. DeWitt and J. Peyraud (Gordon and Breach Publishers, New York, 1975), pp. 113–215.

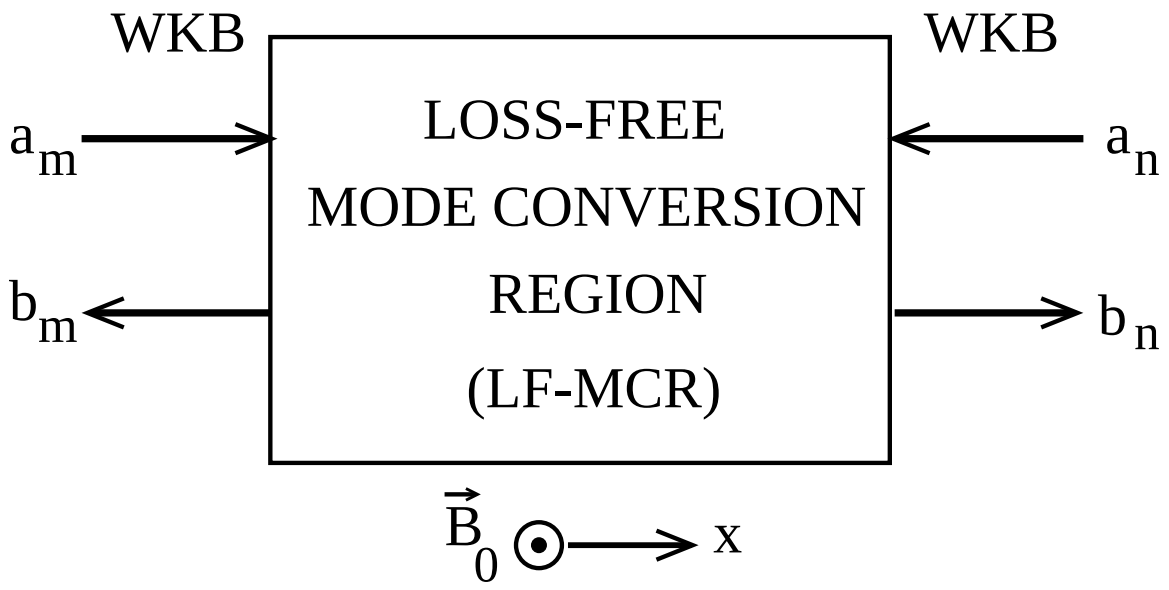

Figure 27. Loss-free mode conversion region with incident and reflected (WKB) waves in adjoining regions.

where $\chi^{H}_{\alpha\beta}$ is the Hermitian part of the susceptibility tensor $\chi_{\alpha\beta}(\vec{k},\omega)$ with $\vec{k}$ and ω real.[31] Since the full-wave equations describing the LF-MCR are linear (in general, linear integro-partial-differential equation) with appropriate boundary conditions, the complex field amplitudes a_p and b_p are related by a unique scattering matrix $\overline{\overline{S}}$

$$\vec{b} = \overline{\overline{S}} \cdot \vec{a} \tag{40}$$

where $\vec{b}$ and $\vec{a}$ are column vectors containing complex amplitudes of all b_p and all a_p, respectively.

From *energy flow conservation* applied to the LF-MCR, we have

$$\Sigma_p \left(\left| a_p \right|^2 - \left| b_p \right|^2 \right) = 0; \quad p = m + n\,, \tag{41}$$

where the sum is over all *m*'s and *n*'s. Using (40), we can express this as

$$\vec{a}^{\dagger} \cdot \left(\overline{\overline{I}} - \overline{\overline{S}}^{\dagger} \cdot \overline{\overline{S}} \right) \cdot \vec{a} = 0\,, \tag{42}$$

where the dagger superscript on $\overline{\overline{S}}$ denotes the complex-conjugate-transpose of $\overline{\overline{S}}$. Since (42) must hold true for arbitrary $\vec{a}$, it follows that

[31] For the explicit form of $\chi_{\alpha\beta}$ for a relativistic plasma with arbitrary equilibrium distribution function, see e.g., G. Bekefi, *Radiation Processes in Plasmas* (John Wiley & Sons, 1966), Section 7.2; and T. H. Stix, *Waves in Plasmas* (New York: American Institute of Physics, 1992), Chapter 10.

$$\overline{\overline{S}}^{\dagger} = \overline{\overline{S}}^{-1}. \tag{43}$$

Next, consider *wave energy flow under time reversibility of the dynamics*. For the time reversed system, the direction of time-averaged energy flow density changes sign. In other words, the reversal of time changes time-averaged energy flow *into* the mode conversion region to time-averaged energy flow *out* of the mode conversion region, and vice versa. From (2), energy flow reversal is obtained by setting[32]

$$\vec{E} \to \vec{E}^{*}; \quad \vec{H} \to -\vec{H}^{*}; \quad k_x \to -k_x \tag{44}$$

and thus, by (35) and (36), changing

$$a_p \to b_p^{*} \quad \text{and} \quad b_p \to a_p^{*}, \tag{45}$$

where the star superscript denotes the complex conjugate. Referring to Figure 27, the effect of time reversal is to change *a* to *b** and *b* to *a**, with arrows pointing in the same direction as indicated in the figure. Thus

$$\vec{a}^{*} = \overline{\overline{S}} \cdot \vec{b}^{*} \tag{46}$$

or, taking the complex conjugate of (46),

$$\vec{a} = \overline{\overline{S}}^{*} \cdot \vec{b}. \tag{47}$$

But from (40) $\vec{a} = \overline{\overline{S}}^{-1} \cdot \vec{b}$; hence

$$\overline{\overline{S}}^{*} = \overline{\overline{S}}^{-1}. \tag{48}$$

Combining (43) and (48), we finally obtain:

$$\overline{\overline{S}}^{\dagger} = \overline{\overline{S}}^{*} \quad \text{or equivalently} \quad \overline{\overline{S}}^{T} = \overline{\overline{S}}, \tag{49}$$

where the *T* superscript on $\overline{\overline{S}}$ denotes the transpose of $\overline{\overline{S}}$. Hence, *the LF-MCR scattering matrix is symmetric*.

The symmetry of the LF-MC scattering matrix, $S_{ij} = S_{ji}$, entails important relationships for various power coefficients of the mode conversion process:

[32] Note: for real $\vec{k}$ and ω, $\chi^{H}_{\alpha\beta}\left(-\vec{k},\omega\right) = \chi^{H}_{\alpha\beta}\left(\vec{k},\omega\right)$ for any kinetic (Vlasov) description of a plasma in a magnetic field and with an equilibrium momentum distribution function symmetric in parallel (to the magnetic field) momentum; see references in previous footnote.

$$\left|S_{ij}\right|^2 = \left|\frac{b_i}{a_j}\right|^2 = \left|\frac{b_j}{a_i}\right|^2 = \left|S_{ji}\right|^2 . \tag{50}$$

Thus:

(a) For disparate modes on the two sides of the LF-MCR, the *mode conversion power coefficients* are equal.

(b) For disparate modes on the same side of the LF-MCR, the *reflection* (they are in essence also mode conversion) *power coefficients* are equal.

(c) For the same modes on the two sides of the LF-MCR, the *transmission power coefficients* are equal.

We illustrate these with examples of MC occurring in plasmas in a magnetic field, relevant to toroidally confined plasmas. In the following examples, the MCR occurs between the low density, low magnetic field side, toward the outside of the plasma, and the higher density, higher magnetic field toward the inside of the plasma. In all cases, the frequency and wave number in the *z*-direction is assumed given by the excitation source. Finally, we generalize our results to propagation in 3-D.

A. *Mode Conversion of Fast Alfvén Wave (FAW) to Ion-Bernstein Wave (IBW) at the Ion-Ion Hybrid Resonance (IIHR)*

We assume conditions such that the individual ion-cyclotron resonances are outside the MCR containing the IIHR. Thus, the MCR under consideration is loss-free (LF). Two types of scenarios are possible in this mode conversion, depending upon whether a cutoff follows the IIHR within the MCR or not.

1) *Cutoff following IIHR within MCR.*[33]

The local dispersion relation in the LF-MCR, and the WKB modes outside its boundaries, are illustrated in Figure 28; the associated scattering matrix is given by:

$$\begin{pmatrix} b_B \\ b_F \end{pmatrix} = \begin{pmatrix} S_B & S_{FB} \\ S_{BF} & S_F \end{pmatrix} \begin{pmatrix} a_B \\ a_F \end{pmatrix} . \tag{51}$$

The symmetry condition (49) gives $S_{FB} = S_{BF}$, i.e., the power coefficient for the excitation of the IBW by a FAW, $|S_{FB}|^2$, is the same as the power coefficient for the excitation of a FAW from an IBW, $|S_{BF}|^2$; the former is important to heating with a FAW excitation, while the latter is relevant to emission from IBWs and thus useful in diagnosing energetic ion (e.g., fusion α's on which IBWs damp) temperatures. Note that the time reversibility condition (48) also gives $S_B = S_F$; this entails a power reflectivity symmetry: $|S_B|^2 = |S_F|^2$.

[33] In the cold plasma limit, when the IBW branch in Figure 28 does not exist, the local dispersion relation has a resonance ($k_x \to \infty$ at the IIHR) that connects to the cutoff on the high n_0, B_0 side of the IIHR. This mode conversion/resonance absorption problem has been solved analytically [see A. K. Ram, A. Bers, S. D. Schultz, and V. Fuchs, "Mode Conversion of Fast Alfvén Waves at the Ion-Ion Hybrid Resonance," *Phys. Plasmas,* **3**, 1976 (1996)].

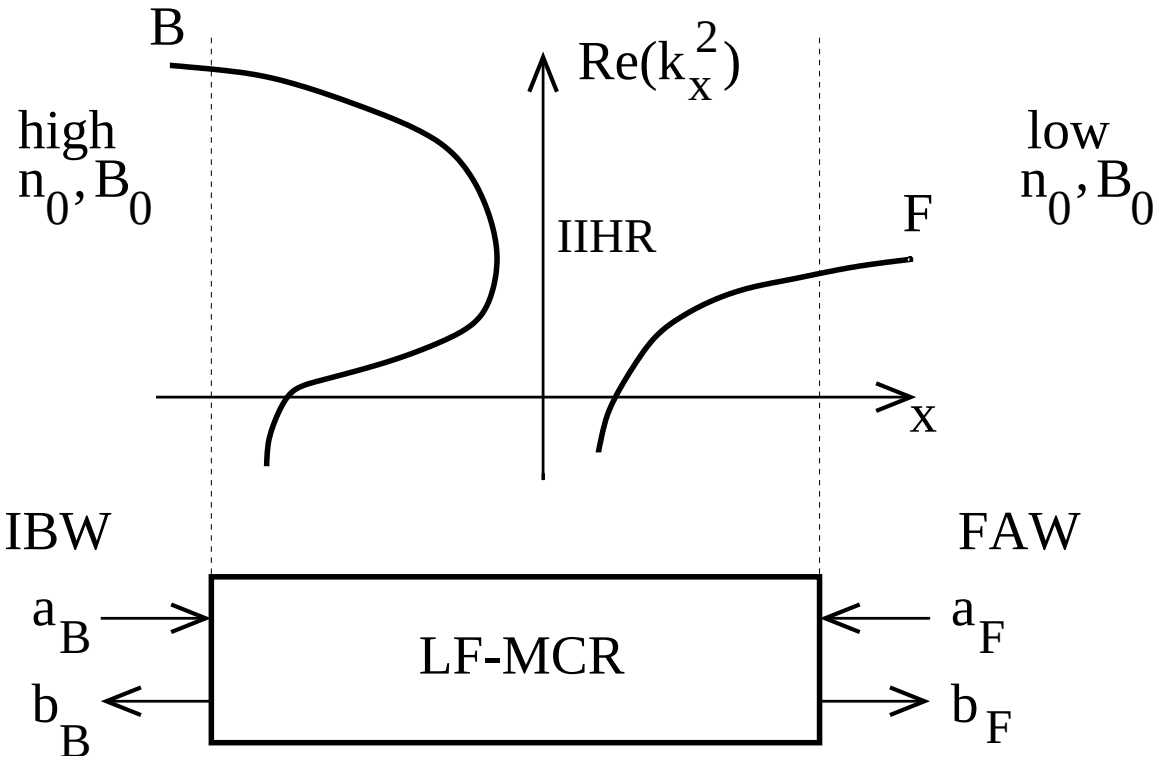

Figure 28. Sketch of the local dispersion relation, for given (ω, k_z) of the FAW-IBW mode conversion; the cutoff is on the high n_0, B_0 side of IIHR, inside the LF-MCR.

2) *Cutoff following IIHR not in MCR.*[34]

The local dispersion relation in the LF-MCR and the boundaries of the LF-MCR with WKB mode fields outside of its boundaries are shown in Figure 29; the associated scattering matrix is given by:

$$\begin{pmatrix} b_B \\ b_H \\ b_L \end{pmatrix} = \begin{pmatrix} S_B & S_{BH} & S_{BL} \\ S_{HB} & S_H & S_{HL} \\ S_{LB} & S_{LH} & S_L \end{pmatrix} \begin{pmatrix} a_B \\ a_H \\ a_L \end{pmatrix}. \tag{52}$$

Here the symmetry condition (49) gives $S_{BH} = S_{HB}$, $S_{BL} = S_{LB}$, and $S_{HL} = S_{LH}$. The first entails that the mode conversion power to the IBW from a FAW incident from the high-field side, $|S_{BH}|^2$, is the same as the mode conversion power to the high-field side FAW from an IBW, $|S_{HB}|^2$ (related to emission from the IBW to high-field side FAW). The second implies that the mode conversion power to the IBW from a FAW excitation on the low-field side, $|S_{BL}|^2$, is the same as the mode conversion power to the low-field side from an IBW, $|S_{LB}|^2$ (related to emission from the IBW to the low-field side FAW).

[34] This is the kinetic modification of the classical Budden resonance-tunnelling problem [K. G. Budden, Section 19.6, "Resonance Tunnelling," in *The Propagation of Radio Waves* (Cambridge University Press, Cambridge, U.K., 1985)] which considers a cold plasma; in that case, the IBW branch in Figure 29 does not exist and there is a resonance ($k_x \to \infty$ at the IIHR) that connects to the FAW on the high n_0, B_0 side. The kinetic problem was approximately solved by many authors [see e.g., Y. C. Ngan and D. G. Swanson, "Mode Conversion and Tunneling in an Inhomogeneous Plasma," *Phys. Fl.,* **20**, 1920 (1977)].

The third entails the equality of the FAW power transmission from the low-field side to the high-field side and the reverse, i.e., $|S_{HL}|^2 = |S_{LH}|^2$.

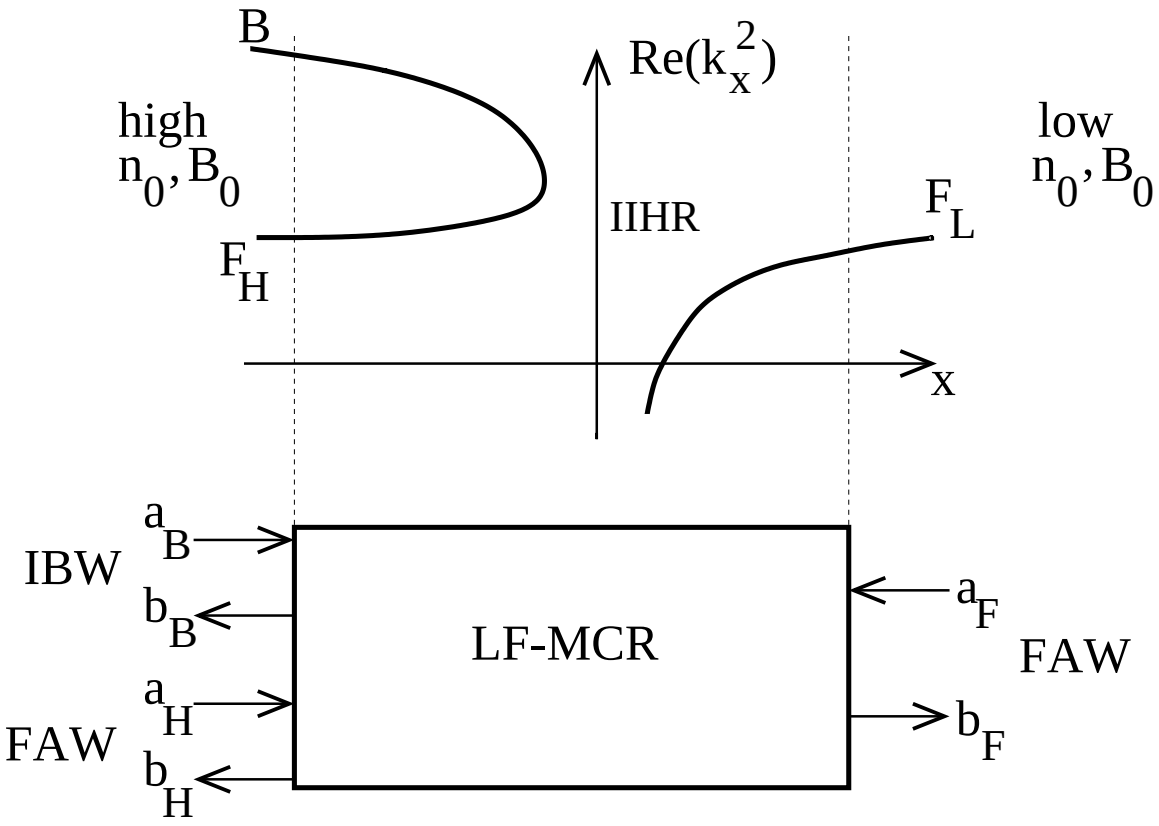

Figure 29. Sketch of the local dispersion relation, for given (ω, k_z) of the FAW-IBW mode conversion; no cutoff on the high n_0, B_0 side of IIHR, inside the LFMCR.

B. *Mode Conversion of O and/or X Modes to Electron Bernstein Waves (EBW) at the Upper-Hybrid Resonance (UHR)*

Here we assume that the Doppler-shifted electron cyclotron resonance is outside the MCR containing the UHR, and thus the MCR is taken as loss-free. We also consider an example of situations relevant to high-β plasmas where the slow X-mode cutoff occurs inside the MCR,[35] as illustrated by the local dispersion relation in Figure 30. The local dispersion relation in Figure 30 is sketched for two sets of values for (ω, k_z) to indicate important differences in the two optimal couplings through MC: X-EBW and O-EBW. The scattering matrix is given by:

[35] A. Bers, A. K. Ram, and S. D. Schultz, "Coupling to Electron Bernstein Waves in Tokamaks," in *Proceedings of the Second Europhysics Topical Conference on RF Heating and Current Drive of Fusion Devices,* Brussels, Belgium, January 20–23, 1998, eds. J. Jacquinot, G. Van Oost, and R. R. Weynants (Contributed Papers, European Physical Society, Vol. 22A, Petit-Lancy, Switzerland), pp. 237–240; A. K. Ram and S. D. Schultz, "Excitation, Propagation, and Damping of Electron Bernstein Waves in Tokamaks," *Phys. Plasmas,* **7**, 4084 (2000); and A. K. Ram, A. Bers, and C. N. Lashmore-Davies, "Emission of Electron Bernstein Waves in Plasmas," *Phys. Plasmas,* **9**, 409 (2002).

$$\begin{pmatrix} b_B \\ b_X \\ b_O \end{pmatrix} = \begin{pmatrix} S_B & S_{BX} & S_{BO} \\ S_{XB} & S_X & S_{XO} \\ S_{OB} & S_{OX} & S_O \end{pmatrix} \begin{pmatrix} a_B \\ a_X \\ a_O \end{pmatrix}. \tag{53}$$

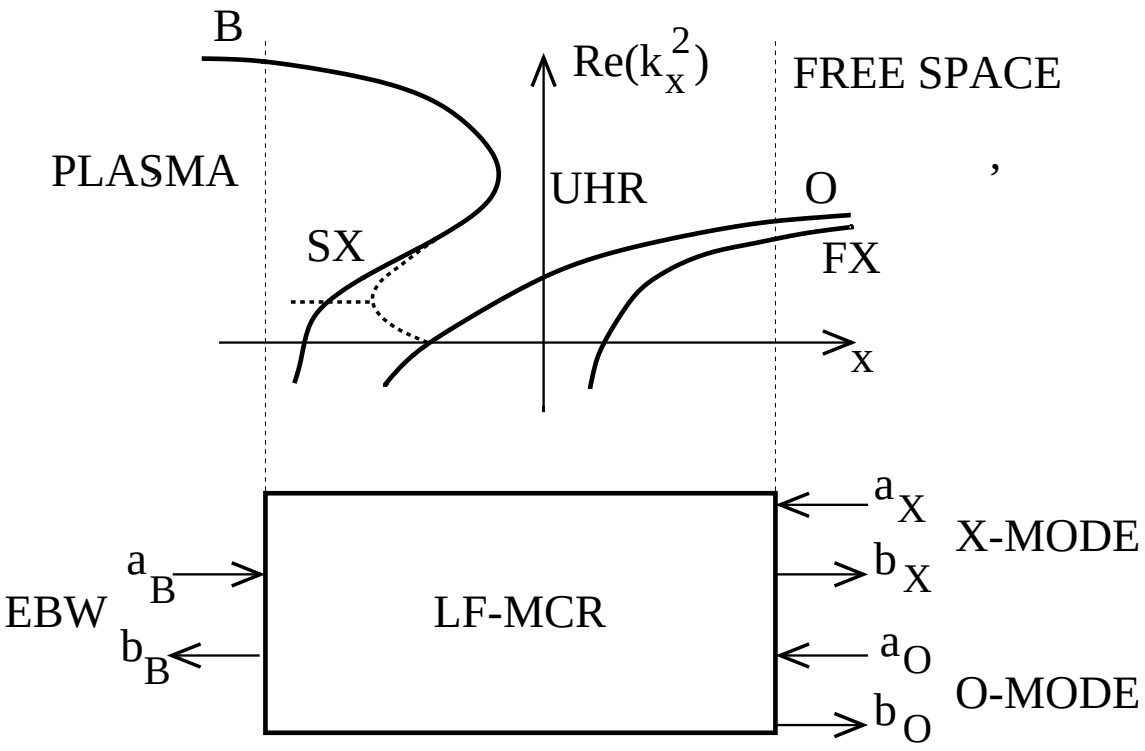

Figure 30. Sketch of the local dispersion relation for O-X-EBW mode conversion near UHR. Two (ω, k_z) situations are depicted; solid line for a case when the O-mode cutoff is well-separated from the SX cutoff, and solid line with SX branch modified as shown by dashed line when the SX cutoff coincides with the O-mode cutoff.

The symmetries required by (49) give three relations: $S_{BX} = S_{XB}$, $S_{BO} = S_{OB}$, and $S_{XO} = S_{OX}$. The first entails that mode conversion power excitation of EBWs by X-modes is the same as MC power excitation of X-modes by EBWs (emission), $|S_{BX}|^2 = |S_{XB}|^2$. The second is of a similar nature for the O-EBW mode conversion power and EBW emission MC to O-mode, $|S_{BO}|^2 = |S_{OB}|^2$. The last relation states a reflection symmetry: the power reflected into the X-mode by an excitation of the O-mode, $|S_{XO}|^2$, is the same as the power reflected into the O-mode by an excitation of the X-mode, $|S_{OX}|^2$.

An approximate kinetic formulation of the full-wave problem of coupling among O, X, and EBWs near the UHR has been solved computationally (see the last reference in footnote 35). The results exhibit all of the above symmetries exactly.

C. *Mode Conversion Symmetries in 3-D Propagation*

Generalizing to propagation in 3-D, the LF-MCR will be bounded by a surface. Waves in the WKB space outside the LF-MCR will have energy flows into and out of this surface in directions determined by (group velocity) ray tracing. The energy flow density along such a ray is given by

$$\left\langle \vec{s} \right\rangle = \frac{1}{2}\mathrm{Re}(\vec{E}\times\vec{H}^{*}) - \frac{\varepsilon_0}{4}\omega\frac{\partial\chi^{H}_{\alpha\beta}}{\partial\vec{k}}E_{\alpha}E^{*}_{\beta}. \tag{54}$$

The waves on the LF-MCR surface are then uniquely related by a scattering matrix as in (40). Wave energy flow conservation is then expressed identically to (41), giving (43). Wave energy flow under time reversibility of the dynamics is obtained as in (44) with k_x replaced by $\vec{k}$, and $\chi^{H}_{\alpha\beta}\left(-\vec{k},\omega\right)=\chi^{H}_{\alpha\beta}\left(\vec{k},\omega\right)$ as in footnote 32. Thus we arrive at (48) and, together with (43), finally at (49).

Publications

Journal Articles, Published

A. K. Ram, A. Bers, and C. N. Lashmore-Davies, “Emission of Electron Bernstein Waves in Plasmas," *Phys. Plasmas,* **9**, 409 (2002).

D. G. Hicks, C. K. Li, F. H. Seguin, J. D. Schnittman, A. K. Ram, J. A. Frenje, R. D. Petrasso, J. M. Soures, D. D. Meyerhofer, S. Roberts, C. Sorce, C. Stockl, T. C. Sangster, and T. W. Phillips. “Observations of Fast Protons Above 1 MeV Produced in Direct-Drive Laser-Fusion Experiments,” *Phys. Plasmas* **8**, 606 (2001).

S. M. Kaye, M. G. Bell, R. E. Bell, J. Bialek, T. Bigelow, M. Bitter, P. Bonoli, D. Darrow, P. Efthimion, J. Ferron, E. Fredrickson, D. Gates, L. Grisham, J. Hosea, D. Johnson, R. Kaita, S. Kubota, H. Kugel, B. LeBlanc, R. Maingi, J. Manickam, T. K. Mau, R. J. Maqueda, E. Mazzucato, J. Menard, D. Mueller, B. Nelson, N. Nishino, M. Ono, F. Paoletti, S. Paul, Y.-K. M. Peng, C. K. Phillips, R. Raman, P. Ryan, S. A. Sabbagh, M. Schaffer, C. H. Skinner, D. Stutman, D. Swain, E. Synakowski, Y. Takase, J. Wilgen, J. R. Wilson, W. Zhu, S. Zweben, A. Bers, M. Carter, B. Deng, C. Domier, E. Doyle, M. Finkenthal, K. Hill, T. Jarboe, S. Jardin, H. Ji, L. Lao, K. C. Lee, N. Luhmann, R. Majeski, S. Medley, H. Park, T. Peebles, R. I. Pinsker, G. Porter, A. Ram, M. Rensink, T. Rognlien, D. Stotler, B. Stratton, G. Taylor, W. Wampler, G. A. Wurden, X. Q. Xu, and L. Zeng. “Initial Physics Results From the National Spherical Torus Experiment,” *Phys. Plasmas* **8**, 1977 (2001).

Journal Articles, Submitted for Publication

R. J. Focia, D. S. Montgomery, J. C. Fernández, and R. P. Johnson, “Observation of Multiple Cascade Steps of the Langmuir Decay Instability in a Laser Plasma,” submitted to *Phys. Rev. Lett.*

Meeting Papers, Published

A. Bers and A. K. Ram, “General Proof of Symmetries in Mode Conversions,” *Bull. Amer. Phys. Soc.,* **46 (11)**, 19 (2001).

J. Decker, Y. Peysson, A. Bers, and A. K. Ram, "Synergism of RF Current Drive with the Bootstrap Current," *Bull. Am. Phys. Soc.,* **46**, 189 (2001).

R. J. Focia, A. Bers, A. K. Ram, and M. M. Shoucri, "Electron Acoustic Waves Generated in SRS by Beam-Plasma Interaction," *Bull. Am. Phys. Soc.,* **46**, 283 (2001).

A. Hansen, D. Garnier, J. Kesner, M. Mauel, and A. Ram, "ECRH in Levitated Dipole Experiment," *Proceedings of the 14th Topical Conference on Radio Frequency Power in Plasmas,* Oxnard, California, May 7 – 9, 2001, eds. T. K. Mau and J. deGrassie (Melville, New York: A.I.P. Conf. Proc. 595, 2001), pp. 362–365.

A. K. Hansen, D. T. Garnier, M. E. Mauel, J. Kesner, and A. Ram, "Multi-Frequency ECRH on LDX," *Bull. Am. Phys. Soc.,* **46**, 228 (2001).

A. K. Ram and A. Bers, "Electron Bernstein Wave Heating and Emission in Spherical Tokamaks," to appear in *Proceedings of the 2nd IAEA Technical Committee Meeting on Spherical Tori and 7th International Spherical Torus Workshop,* Sao Jose dos Campos, Brazil, August 1 – 3, 2001.

A. K. Ram, A. Bers, C. N. Lashmore-Davies, G. Taylor, and P. Efthimion, "Electron Bernstein Waves in Spherical Tokamaks," *Proceedings of the 28th European Physical Society (EPS) Conference on Controlled Fusion and Plasma Physics,* Funchal, Madeira, Portugal, June 18 – 22, 2001. <http://www.cfn.ist.utl.pt/EPS2001/fin/pdf/P3.070.pdf>

A. K. Ram, A. Bers, and A. Salcedo, "Electric Fields in Density Cavities and the Transverse Energization of Ions," *EOS* (2001 American Geophysical Union Fall Meeting supplement), **82 (47)**, F1084 (2001), Paper SM51B-0819.

A. K. Ram, A. Bers, G. Taylor, and P. Efthimion, "Emission of Electron Bernstein Waves," *Proceedings of the 14th Topical Conference on Radio Frequency Power in Plasmas,* Oxnard, California, May 7 – 9, 2001, eds. T. K. Mau and J. deGrassie (Melville, New York: A.I.P. Conf. Proc. 595, 2001), pp. 434–437.

A. K. Ram, A. Bers, G. Taylor, and P. C. Efthimion, "Emission of Electron Bernstein Waves from NSTX," *Bull. Am. Phys. Soc.,* **46**, 259 (2001).

A. Salcedo, A. Bers, and A. K. Ram, "Space-Time Evolution of SRS Coupled to LDI and the Effect of Ion Acoustic Damping," *Bull. Am. Phys. Soc.,* **46**, 284 (2001).

D. J. Strozzi, A. K. Ram, and A. Bers, "Stochastic Particle Motion due to Multiple Electrostatic Waves," *Bull. Am. Phys. Soc.,* **46**, 275 (2001).

G. Taylor, P. C. Efthimion, B. Jones, J. C. Hosea, R. Kaita, B. P. LeBlanc, R. Majeski, R. Munsat, C. K. Phillips, J. Spaleta, J. R. Wilson, D. Rasmussen, G. Bell, T. S. Bigelow, M. D. Carter, D. W. Swain, J. B. Wilgen, A. K. Ram, A. Bers, R. W. Harvey, and C. B. Forest, "Electron Bernstein Wave Research on CDX-U and NSTX," *Proceedings of the 14th Topical Conference on Radio Frequency Power in Plasmas,* Oxnard, California, May 7 – 9, 2001, eds. T. K. Mau and J. deGrassie (Melville, New York: A.I.P. Conf. Proc. 595, 2001), pp. 282–289.

Reports

R. J. Focia, D. S. Montgomery, J. C. Fernández, and R. P. Johnson, "Observation of Multiple Cascade Steps of the Langmuir Decay Instability in a Laser Plasma," Plasma Science and Fusion Center Report No. PSFC/JA-01-17, (Cambridge, Massachusetts: Massachusetts Institute of Technology, 2001).

A. K. Ram, A. Bers, and C. N. Lashmore-Davies, "Emission of Electron Bernstein Waves in Plasmas," Plasma Science and Fusion Center Report No. PSFC/JA-01-32, (Cambridge, Massachusetts: Massachusetts Institute of Technology, 2001).

A. K. Ram, A. Bers, G. Taylor, and P. Efthimion, "Emission of Electron Bernstein Waves," Plasma Science and Fusion Center Report No. PSFC/JA-01-35, (Cambridge, Massachusetts: Massachusetts Institute of Technology, 2001).

A. K. Ram, A. Bers, C. N. Lashmore-Davies, G. Taylor, and P. Efthimion, "Electron Bernstein Waves in Spherical Tokamaks," Plasma Science and Fusion Center Report No. PSFC/JA-01-36, (Cambridge, Massachusetts: Massachusetts Institute of Technology, 2001).

A. K. Ram and A. Bers, "Electron Bernstein Wave Heating and Emission in Spherical Tokamaks," Plasma Science and Fusion Center Report No. PSFC/JA-01-37, (Cambridge, Massachusetts: Massachusetts Institute of Technology, 2001).

Theses

R. J. Focia, *Observation and Characterization of Single Hot Spot Laser-Plasma Interactions*, Ph.D. dissertation, Department of Electrical Engineering and Computer Science, MIT, February 2002.

A. Salcedo, *Coupled Modes Analysis of SRS Backscattering, with Langmuir Decay and Possible Cascadings,* Ph.D. dissertation, Department of Electrical Engineering and Computer Science, MIT, December, 2001.